Acta Crystallographica Section A
Foundations of Crystallography
ISSN 0108-7673

Received 27 April 2004
Accepted 16 September 2004

Transmission electron microscopy and structural phase transitions in anion-deficient perovskite-based oxides

Joke Hadermann,[a]* Gustaaf Van Tendeloo[a] and Artem M. Abakumov[b]

[a]EMAT, University of Antwerp, Groenenborgerlaan 171, B-2020 Antwerp, Belgium, and [b]Department of Chemistry, Moscow State University, Moscow 119992, Russia. Correspondence e-mail: joke.hadermann@ua.ac.be

This review deals with the structural transitions arising in anion-deficient Mn- and Cu-based perovskites when changing the anion content. Special attention is devoted to the local structure of such materials, studied with electron diffraction and high-resolution electron microscopy. Using examples of three-dimensional or layered manganites and cuprates, it is shown that oxidation/reduction reactions in such compounds are accompanied by the formation of domain structures. Fragmentation into domains can have intrinsic reasons, related to the loss of symmetry elements due to the ordering of anion vacancies, or because of the simultaneous realization of several different anion ordering patterns with close formation energies. When extra anions are inserted at low temperatures, limited diffusion ability also results in the appearance of domains of different structures arising from a local inhomogeneity in the anion distribution. The relevance of the investigation of the local structure for a correct structure interpretation is discussed.

1. Introduction

Increasing technological demands inspire an extensive search for new materials possessing a promising industrial value. Modern solid-state chemistry constantly develops new synthesis pathways resulting in numerous fascinating compounds, where the complex oxides of transition metals occupy an important place. Perovskite-based cuprates and manganites receive great attention and are widely studied due to the discovery of high-temperature superconductivity (cuprates) and colossal magnetoresistive properties (manganites). Apart from practical applications, these oxides are interesting from a fundamental point of view because of their rich variety of magnetic properties and the complex interplay between the magnetic structure, transport properties, crystal structure, chemical composition, charge and orbital ordering phenomena. However, chemists have already realized that the conventional synthesis techniques applicable for the preparation of thermodynamically stable phases (*e.g.* long time annealings at high temperatures for promoting cation diffusion) provide only a limited range of new materials. Modern approaches to the synthesis of inorganic materials, aimed at the preparation of metastable phases (phases not in a thermodynamic equilibrium with the environment) are currently the subject of significant interest. Soft chemistry techniques such as low-temperature intercalation/deintercalation, electrochemical oxidation/reduction, variation of oxygen content or halogen doping, reduction with metal hydrides *etc.* have resulted in a list of new compounds, often looking highly unusual when their thermodynamic stability is discussed. Superconducting $YBa_2Cu_3O_6F_2$ (T_c = 94 K) (Van Tendeloo *et al.*, 1997; Abakumov *et al.*, 2002) and $Hg_{0.8}Ba_2Ca_2Cu_{3.2}O_8F_\delta$ (T_c = 138 K) (Lokshin *et al.*, 2001; Abakumov *et al.*, 2002) oxyfluorides synthesized by low-temperature fluorination with XeF_2 are among such compounds. The preparation of these materials using routine ceramic techniques would result in the formation of BaF_2 having an extremely high lattice energy. Another example is the transition-metal oxide hydride $LaSrCoO_3H_{0.7}$, prepared by a reaction of $LaSrCoO_4$ with CaH_2, that adopts an unprecedented structure in which oxide chains are bridged by hydride anions to form a two-dimensional extended network in which magnetic ordering is found up to at least 350 K (Hayward *et al.*, 2002; Blundell *et al.*, 2003). This material is unstable with respect to decomposition into a mixture of oxides with the partial reduction of Co down to cobalt metal. In addition to these examples, many other similar compounds can be listed. Since in many cases the soft chemistry reactions are carried out at temperatures that are too low for effective cation migrations, the anion sublattice appears to be affected first, leaving the cation sublattice roughly unaltered. This matches with the requirement to keep the reaction within the conditions of kinetic stability of the primary structure.

If the targeted compound can be prepared at equilibrium conditions, good quality samples are usually available for the subsequent investigation by different diffraction techniques:

doi: 10.1107/S0108767304023013

either small single crystals suitable for X-ray diffraction experiments or large bulk samples for high-quality high-resolution powder neutron diffraction. However, the samples prepared by soft chemistry techniques often do not meet these criteria. For instance, Reller *et al.* (1985) surmized that the difficulties hampering the structural investigation of the topotactically reduced $CaMnO_{3-\delta}$ and $Ca_2MnO_{4-\delta}$ phases arise from the microcrystalline character of the initial material necessary for the preparation of the homogeneous reduced samples with defined stoichiometry and the lack of sufficiently large crystalline domains in the final phase. Nevertheless, the same questions always return: what is the true crystallographic symmetry of the structure? Are the anions ordered or randomly distributed? What is the local structure of the material and is it chemically homogeneous? This paper aims to show that transmission electron microscopy (TEM) is an effective technique for such structural investigations, due to its sensitivity to the lighter elements such as oxygen and its ability to provide structural information at local level down to atomic scale. In TEM, atomic scale real-space (high-resolution electron microscopy, HREM) and reciprocal-space (electron diffraction, ED) investigations can be combined with compositional analyses using energy-dispersive X-ray analysis (EDX) and electron-energy-loss spectroscopy (EELS). Using the latter, it is possible to map chemical and bonding information at the atomic scale (Browning *et al.*, 1993; Batson, 1993; Muller *et al.*, 1993, 1995). Scanning transmission electron microscopy (STEM) can, although not discussed in the present paper, also directly be used for studying oxygen vacancy ordering. Using this technique, Stemmer *et al.* (2000) for $SrCoO_{3-\delta}$, and Klie *et al.* (2001) and Klie & Browning (2002) for $(La_xSr_{1-x})(Fe_yCr_{1-y})O_{3-\delta}$, $SrCoO_{3-\delta}$ and $SrTiO_3$ have used Z contrast to determine the ordering of oxygen vacancies in these materials. A review of TEM work on high-temperature copper-based oxide superconductors can be found in Matsui & Akimitsu (1995). Elaborate reviews of the general progress in TEM/STEM can be found in Muller & Mills (1999), Spence (1999) and Sinnott & Dickey (2003).

It is beyond the scope of this paper to provide a complete review of anion-deficient perovskites and discuss all possible defects and their ordering schemes, which can be partially found in the references (Burdett & Kulkarni, 1988; Raveau *et al.*, 1989; Anderson *et al.*, 1993; Karppinen & Yamauchi, 2000). The present examples of Mn- or Cu-containing anion-deficient perovskite-based materials are aimed to show the interplay between anion content, crystal structure and local structure of such compounds, with the help of TEM.

The aspect 'structural phase transition' can be considered in a strict sense or in a broader sense. In the strict sense, a phase transition is regarded as a structural modification of a compound with fixed composition when changing temperature or pressure. In that case, symmetry elements of the product phase (low temperature) are already present in the parent phase (high temperature). In other words, the low-symmetry phase is characterized by a 'broken symmetry' of the high-temperature phase (Salje, 1990). A lowering of symmetry induces the possible appearance of orientation variants and translation variants. Their number and their relationship can be easily deduced considering either the point-group symmetry (Van Tendeloo & Amelinckx, 1974) or the space-group symmetry (Portier & Gratias, 1982). For example, when a cubic crystal undergoes a phase transition to a tetragonal structure with a doubled c axis, there will be three orientation variants (the tetragonal c axis can be along any of the cubic directions) and two translation variants (the origin can be at either 0,0,0 or 0,0,1/2). Between the different variants, domain boundaries will be created. Between orientation variants, these domain boundaries are called twin boundaries or inversion boundaries; between translation variants, they are called out-of-phase boundaries (Van Tendeloo & Amelinckx, 1974).

In the present contribution, we will use the term 'phase transition' in a broader sense. In perovskite-based materials, we have a framework of cations and anions with an ideal composition ABO_3. We will leave the cation sublattice unaltered but allow slight deviations in composition of the anion framework. This will also introduce symmetry changes, but neighboring 'domains' might have a different anion arrangement and/or composition. Nevertheless, we will continue calling these boundaries 'domain boundaries'.

2. Mn- and Cu-containing anion-deficient perovskite-based materials

In complex oxides, Mn^{3+} and Cu^{2+} cations show similar crystal chemistry behavior. To some extent, the size factor is important: the ionic radii of these cations in an octahedral oxygen environment are close [$r(Mn^{3+})$ = 0.79 Å, $r(Cu^{2+})$ = 0.87 Å]. However, the main feature that determines this similarity is the ability to adopt distorted oxygen coordination due to a Jahn–Teller effect. Mn^{3+} in a high-spin state ($t_{2g}^3e_g^1$) and Cu^{2+} ($t_{2g}^6e_g^3$) surrounded by an octahedron of O atoms in many cases tend to form four short strong equatorial metal—oxygen bonds and two much longer weak apical ones. A progressive apical elongation of the BO_6 (B = Mn, Cu) octahedron can lead to the removal of one apical O atom with the formation of a tetragonal pyramid BO_5. If both apical O atoms are removed, the B cation adopts a square-planar coordination, which is often observed for Cu^{2+} but is not found in the complex oxides containing Mn^{3+}. For the Cu atoms, further reduction of the coordination number is possible and is related to decreasing the oxidation state down to +1 at which Cu usually has a dumbbell coordination. Owing to these features, the Cu- and Mn-containing perovskites easily adopt an anion deficiency, and at a significant concentration of anion vacancies form new anion-deficient structures with an ordered arrangement of O atoms and vacancies. Such $ABO_{3-\delta}$ (B = Mn, Cu) perovskites contain $BO_{2-\delta}$ layers of metal–oxygen polyhedra where the coordination number for some metal atoms is less than 6. This approach has several limitations. For example, anion-deficient hexagonal perovskites are more conveniently described as the insertion of hexagonal $AO_{3-\delta}$ layers between the close-packed AO_3 ones. $BaMnO_{3-\delta}$ has a hexagonal $2H$ close-packed structure of BaO_3 layers with Mn cations in the octahedral interstices, and upon reducing the oxygen content this structure transforms into different stacking variants by a replacement of 'hexagonal' BaO_3 layers by anion-deficient $BaO_{2.5}$ 'cubic'-type ones. The anion vacancies in the $BaO_{2.5}$ layers are arranged in such a way that part of the MnO_6 octahedra are transformed into MnO_5 square pyramids. For $0 < \delta \le 0.1$, the oxygen deficiency is accommodated by the formation of ordered 15*R* and 21*R* rhombohedral phases; at $0.22 < \delta \le 0.25$, the disordered intergrowths of hexagonal polytypes are found, and $\delta = 0.25$ corresponds to an ordered 4*H* phase (Parras *et al.*, 1995). A virtual separation of the anion-deficient $BO_{2-\delta}$ layers perpendicular to the fourfold axis of the perovskite subcell provides a transparent description of the anion ordering in a large group of cuprates and manganites of alkali-earth and rare-earth metals. Anion deficiency in the $BO_{2-\delta}$ layers is associated with a formation of rows of O-atom vacancies passing perpendicular to the layer. If the ratio between the amounts of O-atom rows and vacant rows is n/m, the δ value in $BO_{2-\delta}$ can be expressed as $\delta = 2/(1+n/m)$. An additional ability to reduce the number of O atoms in the structure (whenever required by synthesis conditions stabilizing a certain oxidation state of Mn or Cu) arises from the possibility to introduce anion vacancies into the $AO_{1-\gamma}$ layers positioned above and below the $BO_{2-\delta}$ layers. The exact pattern of metal–oxygen polyhedra (octahedra, tetragonal pyramids, tetrahedra, squares and dumbbells) is governed by the amount and distribution of O-atom vacancies in such anion-deficient layers. These polyhedra form two-dimensional sheets, chains or clusters being linked through common O atoms. Representative examples of such ordering patterns are given below in order of subsequent decrease of the δ and γ values in the general $AO_{1-\gamma} + BO_{2-\delta} = ABO_{3-\delta-\gamma}$ formula. Symmetry trees will be provided to clarify the relationships between the space groups of the ordered anion-deficient structures and the space symmetry of the parent perovskite aristotype.

Removal of one quarter of the O atoms from the BO_2 layer ($\delta = 0.5$, $\gamma = 0$, $n/m = 3$) results in a decrease of the average coordination number of the *B* cations down to 5. If all the BO_6 octahedra are transformed into BO_5 tetragonal pyramids linked by common corners, the crystal structure of $Ca_2Mn_2O_5$ (Poeppelmeier *et al.*, 1982) is formed (Fig. 1*a*). Along with this structure, the $Sr_2Mn_2O_5$ (Caignaert *et al.*, 1985), $Sr_2Mn_{2-x}Ti_xO_{5+x/2}$ (Caignaert *et al.*, 1986), $(La,Sr)_4Cu_4O_{10}$ (Otzschi & Ueda, 1993) and $La_{0.816}Sr_{0.184}CuO_{2.5}$ (Hiroi, 1996) compounds can be mentioned as having the same ordering pattern of tetragonal pyramids. The ordering pattern of the vacant oxygen chains is presented schematically in Fig. 1(*b*); these structures all have *Pbam* space symmetry. The transformation from the ideal perovskite structure to this anion-deficient structure follows the maximal group–subgroup symmetry tree: $Pm\bar{3}m$ $(\mathbf{a},\mathbf{b},\mathbf{c}) \rightarrow P4/mmm$ $(\mathbf{a},\mathbf{b},\mathbf{c}) \rightarrow P4/mbm$ $(2(-\mathbf{a}+\mathbf{b}),2(\mathbf{a}+\mathbf{b}),\mathbf{c}) \rightarrow Pbam$ $(2(-\mathbf{a}+\mathbf{b}),(\mathbf{a}+\mathbf{b}),\mathbf{c})$. $BO_{1.5}$ layers in the $Ca_2Mn_2O_5$ structure do not provide a unique way to form an ordered arrangement of vacant oxygen rows keeping a tetragonal pyramidal coordination environment for the *B* cations. Another type of structure containing *B* cations uniquely in BO_5 pyramids is $Sr_2MnO_{3.5}$ (Fig. 8) (Gillie *et al.*, 2002) and $Sr_3Mn_2O_{6+x}$ (Gillie *et al.*, 2003); both compounds will be discussed in detail in §3 of this paper.

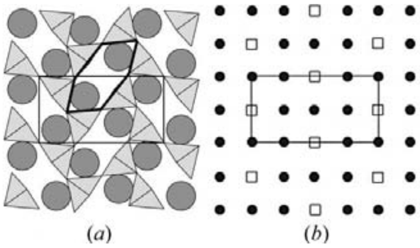

Figure 1
(*a*) Arrangement of metal–oxygen polyhedra in the anion-deficient $BO_{2-\delta}$ layer of $Ca_2Mn_2O_5$. The hexagonal channel is indicated with a black outline. Mn is at the center of the MnO_5 pyramids, O at the corners, Ca is indicated as spheres. The rectangle indicates the borders of the unit cell. (*b*) Ordering pattern of the vacant oxygen chains in this structure.

It is not a necessary requirement to keep the same coordination environment for all cations in the $BO_{1.5}$ ($\delta = 0.5$, $\gamma = 0$, $n/m = 3$) layer. In $La_{8-x}Sr_xCu_8O_{20-\delta}$ ($1.28 \le x \le 1.92$) (Er-Rakho *et al.*, 1988), the major part of the *B* cations stays in tetragonal pyramidal oxygen coordination, since only one out of four nearest neighboring oxygen rows is vacant for the *B* cations of this type (B'). Half of the remaining *B* cations (B'') have no vacant oxygen rows in the neighborhood whereas, for the other half (B'''), two oxygen rows are missing, thus keeping the $BO_{1.5}$ composition of the layer (Fig. 2). The ordering

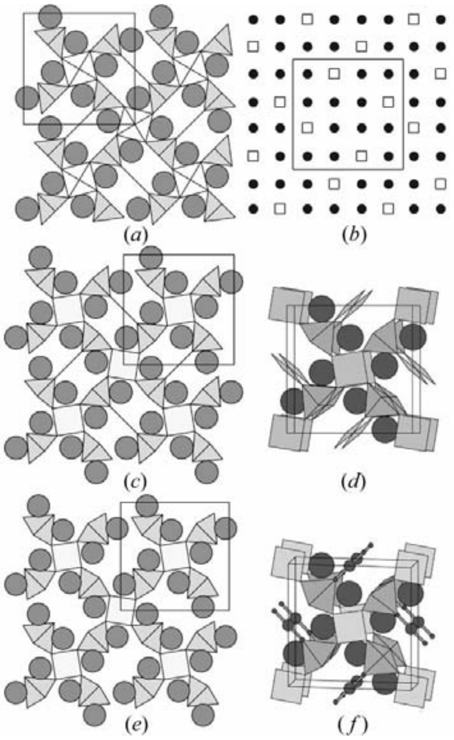

Figure 2
Structure of (*a*) $La_{8-x}Sr_xCu_8O_{20-\delta}$; (*c*) and (*d*) $(La,Sr)_8Cu_8O_{18}$; (*e*) and (*f*) $La_2Sr_6Cu_8O_{16}$. Cu is found at the centers of the polyhedra, O at the corners, the circles represent the positions of La and Sr. (*b*) The ordering pattern of the vacant oxygen chains in the anion-deficient $BO_{2-\delta}$ layer, common for the three compounds.

pattern of vacant oxygen chains is presented schematically in Fig. 2(*b*). The B'' and B''' cations adopt octahedral and square-planar coordination, respectively. In this structure, the B'' and B''' cations form a chess-board pattern. The same ordering as for this compound can also be found in $La_{6.4}Sr_{1.6}Cu_{8-x}Fe_xO_{20}$ ($0 \le x \le 1.20$) and $La_{6.4-x}Sr_{1.6+x}Cu_{8-x}Fe_xO_{20}$ ($0 \le x \le 2$) (Genouel *et al.*, 1995), $(RE_{1-x}Sr_x)_8Cu_8O_{20}$ with RE = Pr (x = 0.35) and RE = Nd (x = 0.40) (Amamoto *et al.*, 1996) and $La_{8-x}Ca_xCu_{8-y}Ni_yO_{20}$ (Roberts *et al.*, 1996). Compounds belonging to this type have space group $P4/mbm$. The unit cell is related to that of the perovskite basic structure as $a \simeq 2a_p2^{1/2}$, $c \simeq a_p$, with a maximal group–subgroup symmetry tree of $Pm\bar{3}m$ $(\mathbf{a},\mathbf{b},\mathbf{c}) \rightarrow P4/mmm$ $(\mathbf{a},\mathbf{b},\mathbf{c}) \rightarrow P4/mbm$ $(2(-\mathbf{a}+\mathbf{b}), 2(\mathbf{a}+\mathbf{b}),\mathbf{c})$. $La_6BaYCu_8O_{20}$ (Cava *et al.*, 1994) (Fig. 3) is built according to the same principles, but with a different ordering pattern of the B'' and B''' cations. $La_{8-x}Sr_xCu_8O_{20-\delta}$ provides the basis for a series of structure types of further reduced compounds through the removal of O atoms from the AO layers (increasing γ). The missing O atoms in the $AO_{1-\gamma}$ layers are located below and above the B'' and B''' cations, transforming their coordination polyhedra from octahedra and squares to squares and dumbbells, respectively. $(La,Sr)_8Cu_8O_{18}$ (Otzschi *et al.*, 1995) (Figs. 2*c*, *d*) (γ = 0.25) consists of a combination of $B''O_4$ and $B'''O_4$ squares and $B'O_5$ pyramids. The square plane for the B'' cation is aligned parallel to the $BO_{1.5}$ layer, and for the B''' cations the squares are perpendicular to the layer. $La_2Sr_6Cu_8O_{16}$ (Fujishita *et al.*, 1991; Fu *et al.*, 1992) (Figs. 2*e*, *f*) (γ = 0.5) is progressively derived from $(La,Sr)_8Cu_8O_{18}$ by removing two O atoms from the $B'''O_4$ squares, resulting in $B'''O_2$ dumbbells. To make the difference clear between the two structures, a clinographic view of the unit cell is shown for both materials, in Figs. 2(*d*) and 2(*f*), respectively. So far this ordering pattern has only been reported for cuprates and not for manganites.

Decreasing δ causes the appearance of octahedra in the array of tetragonal pyramids. $(La,Ba)_5Cu_5O_{13}$ (Michel *et al.*, 1985, 1987) (δ = 0.4, γ = 0, n/m = 4) consists of clusters of four corner-linked $B'O_5$ pyramids linked through single $B''O_6$ octahedra (Fig. 4*a*), its ordering pattern of vacant oxygen rows is shown in Fig. 4(*b*). This type of ordering can be found for the compounds $La_{4+z}Ba_{1-z}Cu_5O_{13+y}$ ($-0.05 \le z \le 0.05$) (Michel *et al.*, 1985, 1987), $SrMnO_{2.6}$ (Leligny *et al.*, 2003), $La_4BaCu_{5-x}M_xO_{13+\delta}$ (M = Fe, Co, Ni) (Shivakumara *et al.*, 1998; Anderson *et al.*, 2003), $(La,Sr)_5Cu_5O_{13}$ (Otzschi *et al.*, 1993) and $La_4BaCu_4CoO_{13.35}$ (Shivakumara *et al.*, 2000). The structure of $La_4BaCu_5O_{12}$ (Rangavittal *et al.*, 1995) is derived from that of $(La,Ba)_5Cu_5O_{13}$ by increasing γ up to 0.2, which removes the apical O atom from the $B''O_6$ octahedron resulting in a $B''O_4$ square-planar coordination (Fig. 4*c*). The symmetry for compounds with this type of ordering pattern is $P4/m$. The relation of these compounds to the perovskite structure is given by the maximal group–subgroup tree $Pm\bar{3}m$ $(\mathbf{a},\mathbf{b},\mathbf{c}) \rightarrow P4/mmm$ $(\mathbf{a},\mathbf{b},\mathbf{c}) \rightarrow P4/m$ $(\mathbf{a}' = 2\mathbf{a} - \mathbf{b}, \mathbf{b}' = \mathbf{a} + 2\mathbf{b}, \mathbf{c}' = \mathbf{c})$, with $a' \simeq a_p$, $b' \simeq a_p5^{1/2}$, $c' \simeq a_p$. Only $La_4BaCu_5O_{12}$ has a lower symmetry ($P2/m$) due to small distortions and tilting of the pyramids. In the $CaMnO_{2.8}$ structure (Reller *et al.*, 1984) (δ = 0.2, γ = 0, n/m = 9), the $B''O_6$ octahedra are linked into zigzag chains which are connected by single $B'O_4$ tetragonal pyramids (Fig. 4*d*). In comparison with the $(La,Ba)_5Cu_5O_{13}$ structure, the point symmetry for $CaMnO_{2.8}$ is lowered to $2/m$ due to the filling of two out of four equivalent vacant oxygen rows, indicated on the structure by *x*.

An example of the anion-deficient structure with $\delta = 0$ and $\gamma = 1$ is given by the 'infinite layer' compounds $ACuO_2$ (A = Ca, Sr, Ba) (Siegrist *et al.*, 1988; Takano *et al.*, 1991) (Fig. 5). In this compound, the Cu atoms reside in square-planar coordination due to complete removal of apical vertexes of the octahedra so that the layer sequence along the fourfold

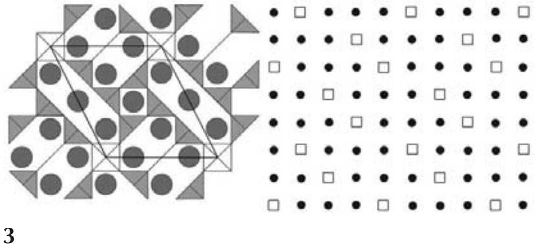

Figure 3
Structure of $La_6BaYCu_8O_{20}$.

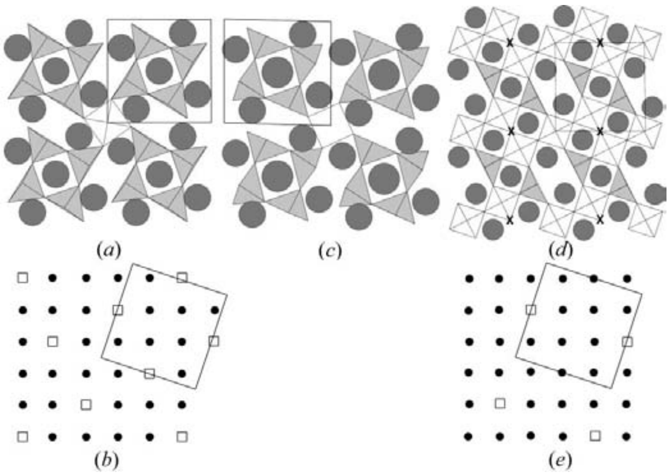

Figure 4
Structure of (*a*) $(La,Ba)_5Cu_5O_{13}$; (*c*) $La_4BaCu_5O_{12}$ and (*d*) $CaMnO_{2.8}$, the crosses indicate the positions of difference in the $BO_{2-\delta}$ layer of the third structure compared to the first two; the ordering pattern of the vacant oxygen chains is given in (*b*) for the first two structures and in (*e*) for the third. These patterns have been rotated in comparison to the structures to allow better comparison with the previous ordering patterns. The unit cell is indicated by a large square.

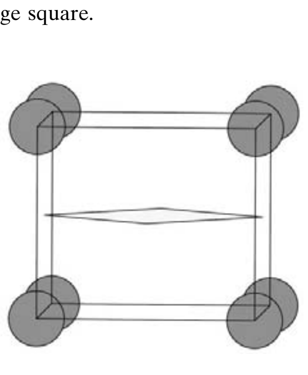

Figure 5
Structural drawing of $ACuO_2$ (A = Ca, Sr, Ba) with Cu at the center of the CuO_4 square and A at the corners of the unit cell.

axis of the perovskite subcell is represented as –CuO_2–A□–CuO_2–.

The perovskite-like anion-deficient layers, organized in a similar way, can also be part of intergrowth structures, such as the Ruddlesden–Popper homologous series where they alternate with the slabs having the rock-salt-type structure. Square coordination of the B cation can be found in Sr_2CuO_3 (Teske & Mueller-Buschbaum, 1969). In this compound, the O atoms and vacancies in the (CuO□) (□-anion vacancy) layer are ordered according to a chessboard pattern. Two O atoms from the (CuO□) layer form two vertices of the CuO_4 squares, whereas two other vertices are formed by O atoms located in the SrO layers positioned above and below the (CuO□) ones. Another structure is found in $Nd_2CuO_{3.5}$ (Pederzolli & Attfield, 1998), where the infinite Cu–O chains are linked by bridging O atoms, through the filling of half of the vacancies in the (CuO□) layer of the Sr_2CuO_3 structure so that these layers acquire ($CuO_{1.5}□_{0.5}$) composition (Fig. 12a).

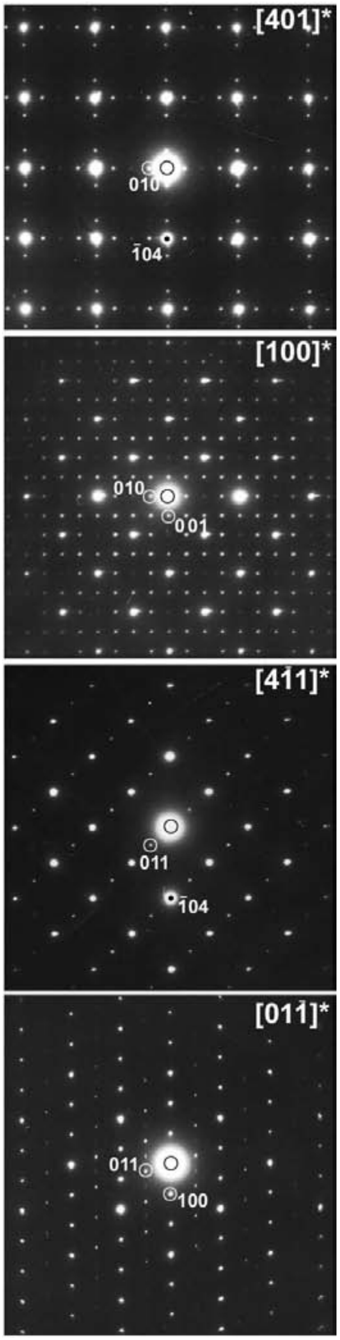

Figure 6
ED patterns for the main zones of $Sr_2MnO_{3.5}$

Another way to introduce anion vacancies into Mn- and Cu-based perovskites is a partial replacement of the transition-metal cations by small cations having a stable tetrahedral environment, such as Ga^{3+} or Al^{3+}. In these compounds, B cations of different type are ordered forming layers, and the anion vacancies are concentrated within the layer of tetrahedrally coordinated cations. Examples of such structures are the brownmillerites $Sr_2MnGaO_{5\pm\delta}$ (Abakumov, Rozova, Pavlyuk, Lobanov, Antipov, Lebedev, Van Tendeloo, Ignatchik *et al.*, 2001; Wright *et al.*, 2001, 2002; Abakumov, Alekseeva *et al.*, 2003; Abakumov, Rozova *et al.*, 2003) and $Ca_2MnGaO_{5+\delta}$ (Abakumov, Rozova, Pavlyuk, Lobanov, Antipov, Lebedev, Van Tendeloo, Sheptyakov *et al.*, 2001), which will be discussed in this paper, $RACuGaO_5$ (R = La, Pr, Nd; A = Ca, Sr) (Vaughey *et al.*, 1991; Roth *et al.*, 1992), $SrCaMnGaO_{5+\delta}$ (Battle *et al.*, 2002), $Y_{0.8}Sr_{2.2}Mn_2GaO_{8-\delta}$ (Gillie *et al.*, 2004), $(Sr_{1-x}Ca_x)_2FeMnO_y$ (x = 0.8–1.0) (Kato *et al.*, 1997) and $Ca_2Sr_2Cu_3GaO_9$ (Khasanova *et al.*, 1996).

The anion-deficient perovskite phases can be prepared from their oxidized analogs by a topotactic low-temperature reduction. In the reverse direction, the anion-deficient phases can be doped with O or halogen atoms, like fluorine, which can be performed under soft conditions. The structural and microstructural consequences of anion intercalation/deintercalation reactions are illustrated below using the examples of the $Sr_2MnO_{3.5}$ and $Sr_3Mn_2O_{6+x}$ Ruddlesden–Popper phases, the fluorinated $Nd_2CuO_{3.5}$ cuprate, and $A_2MnGaO_{5+\delta}$ (A = Ca, Sr) brownmillerites with variable oxygen content.

3. Topotactic reduction of the n = 1 and n = 2 Ruddlesden–Popper (RP) $Sr_{n+1}Mn_nO_{3n+1}$ phases: $Sr_2MnO_{3.5}$ and $Sr_3Mn_2O_{6+\delta}$

The anion-deficient derivatives of the Sr_2MnO_4 ($n = 1$) and $Sr_3Mn_2O_7$ (n = 2) phases were prepared by a solid-state reaction in N_2 flow to stabilize the Mn^{3+} cations. Nevertheless, a subsequent soft reduction with an H_2/N_2 mixture at 823–833 K was necessary to produce the stoichiometric $Sr_2MnO_{3.5}$ and $Sr_3Mn_2O_6$ phases with an Mn-atom formal oxidation state equal to +3. The O-atom non-stoichiometry in the $n = 1$ and $n = 2$ RP materials Sr_2MnO_4 and $Sr_3Mn_2O_7$ has been studied before, but only phases with a disordered array of oxygen vacancies were reported (Kriegel & Feltz, 1992; Mitchell *et al.*, 1999).Transmission electron microscopy revealed that the reduced phases show oxygen–vacancy ordering, whereas this was not obvious on the X-ray powder diffraction patterns.

For $Sr_2MnO_{3.5}$ and $Sr_3Mn_2O_{6+\delta}$, X-ray powder diffraction is consistent with a structure with space group $I4/mmm$ and cell parameters a = 3.81829 (6), c = 12.58165 (19) Å and a = 3.8565 (1), c = 20.2796 (7) Å, respectively. With such unit cells and space symmetry, only a random distribution of the O atoms and vacancies in the $MnO_{1.5}$ layers is possible. However, the Rietveld refinement from neutron diffraction data with a disordered model resulted in unreasonably large reliability factors. Electron diffraction, however, showed for both compounds very bright and sharp superstructure reflections. The ED patterns of the main zones for $Sr_2MnO_{3.5}$ and $Sr_3Mn_2O_{6+\delta}$ are shown in Fig. 6 and Fig. 7, respectively. The ED tilt series for $Sr_2MnO_{3.5}$ revealed this compound to have space group $P2_1/c$ and cell parameters $a \simeq 6.85$, $b \simeq 10.8$, $c \simeq 10.8$ Å, $\beta \simeq 113.2°$. This is related to the body-centered tetragonal subcell by $\mathbf{a} = 1/2(-\mathbf{a}_t - \mathbf{b}_t + \mathbf{c}_t)$, $\mathbf{b} = 2(-\mathbf{a}_t + \mathbf{b}_t)$, $\mathbf{c} = 2(\mathbf{a}_t + \mathbf{b}_t)$. This transformation follows the maximal group–subgroup symmetry tree: $I4/mmm$ $(\mathbf{a}, \mathbf{b}, \mathbf{c}) \rightarrow P4/mmm$ $(2(-\mathbf{a} + \mathbf{b}), 2(\mathbf{a} + \mathbf{b}), \mathbf{c}) \rightarrow P4/mbm$ $(2(-\mathbf{a} + \mathbf{b}), 2(\mathbf{a} + \mathbf{b}), \mathbf{c}) \rightarrow$ $Pbam$ $(2(-\mathbf{a} + \mathbf{b}), 2(\mathbf{a} + \mathbf{b}), \mathbf{c}) \rightarrow P2_1/c$ $(1/2(-\mathbf{a} - \mathbf{b} + \mathbf{c}), 2(-\mathbf{a} + \mathbf{b}), 2(\mathbf{a} + \mathbf{b}))$. New refinements from the powder neutron diffraction data, taking into account the space group and cell deduced from ED data, resulted in the model shown in Fig. 8.

When comparing this structure to that of $Ca_2Mn_2O_5$ (Fig. 1), it is clear that for the current compound the hexagonal channels found in $SrMnO_{2.5}$ and $Ca_2Mn_2O_5$ are elongated. The structure can also be described as consisting of clusters of four corner-sharing pyramids, which are linked by the corners to neighboring clusters. Note that there is no difference between the pattern of the ordering of the vacant O-atom rows for this compound, as shown at the right side of Fig. 8, and the pattern as shown in Fig. 2. However, this compound contains only pyramids as opposed to the mixed polyhedra of the structures in Fig. 2, which is because this pattern of vacant O-atom rows is at a different position relative to the Mn cations for both structural types.

The reduced compound $Sr_2MnO_{3.5}$ exhibits numerous twins, due to the loss of mirror planes and the fourfold axis. An appearance of such twins, obviously related to a decrease of symmetry from $I4/mmm$ down to $P2_1/c$, allows one to assume that the anion ordering to which the twins are related occur either upon cooling of the compound from the temperature of the solid-state reaction or upon the subsequent reduction in the H_2/N_2 gas flow. An ED pattern taken from a twinned domain is shown as the last pattern of Fig. 6. The reflections at $h/2,k,k$ with $h = 2n+1$, $k = 2n+1$ are induced by a twin with a $(100) = (001)_T$ twin plane (T stands for the tetragonal body-centered subcell). This twin occurs due to the loss of the mirror plane perpendicular to the fourfold axis. In the $[401]^* = [001]^*_T$ ED pattern twinning is also observed. The twin plane is $(\bar{1}44) = (100)_T$, and occurs as a result of the loss of the mirror plane perpendicular to the a_T axis. The $Sr_3Mn_2O_{6+\delta}$ phase shows a close relationship with $Sr_2MnO_{3.5}$. Clear superstructure reflections are observed on the ED patterns of $Sr_3Mn_2O_{6+\delta}$ related to oxygen–vacancy ordering which are not detected by X-ray powder diffraction. The supercell has a 10.8×10.8 Å maze with a c parameter of 20.3 Å, in agreement with the c parameter for a structure derived from the $n = 2$ member of the Ruddlesden–Popper series. However, the symmetry of the reduced phase is tetragonal instead of monoclinic as was found for $Sr_2MnO_{3.5}$. To avoid ambiguity because of possible twinning, symmetry analysis on nanometre-sized single domains was performed with microdiffraction (Fig. 9). The extinction symbol was determined to be $P{-}b{-}$, giving three possible space groups: $P4bm$, $P\bar{4}b2$ and $P4/mbm$.

For $Sr_3Mn_2O_{6+\delta}$, the same type of intralayer vacancy ordering is proposed as for $Sr_2MnO_{3.5}$. However, within the restrictions imposed by symmetry and cell dimensions, it is not possible to build a fully ordered model. The ordering scheme suggests a shift of each second anion-deficient bilayer over 1/4[100], as occurs also in $Sr_2MnO_{3.5}$. However, this would require a doubling of the c parameter for $Sr_3Mn_2O_{6+\delta}$, but this was seen neither on the ED patterns nor on the HREM image (Fig. 10). A model that does agree with the cell dimensions and with the symmetry has a random shift of each second bilayer by one of the four equivalent translations, ±1/4[100] and ±1/4[010]. This model is shown in Fig. 11. Owing to the random distribution of the translations, the O-atom occupancies at the $z = 1/2$ layers are equal to $g = 1$, 0.75 and 0.5 at the positions shown in Fig. 11. This model is compatible with the $P4/mbm$ space group, one of the three possibilities found from ED patterns. In this material, no evidence of twinning was found, in agreement with a symmetry reduction from $I4/mmm$ to $P4/mbm$, which maintains the point group $4/mmm$. This random shift model was used for the subsequent refinement of the structure from neutron powder diffraction data. Details of this refinement and the physical properties can be found in Gillie *et al.* (2003). The refinement confirmed the proposed model but revealed a slightly larger oxygen content introduced by a minor aerial oxidation, resulting in the $Sr_3Mn_2O_{6.11}$ composition.

In summary, both $Sr_2MnO_{3.5}$ and $Sr_3Mn_2O_6$ have the same intralayer ordering of O atoms and vacancies, but differ by the stacking of the anion-deficient layers. In $Sr_2MnO_{3.5}$,

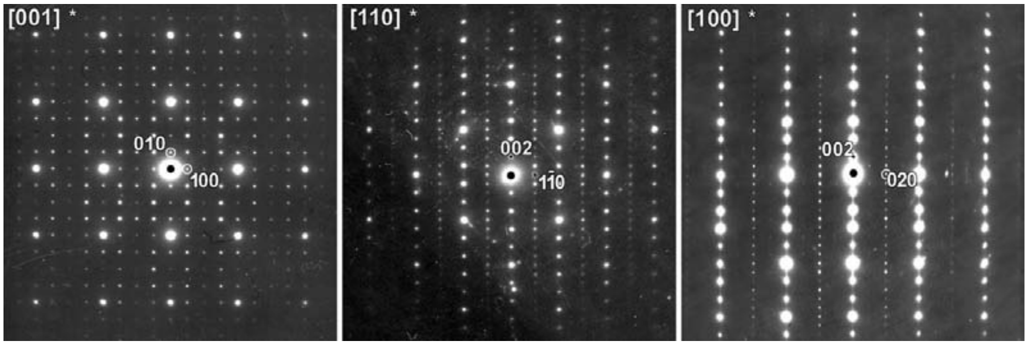

Figure 7
ED patterns for the main zones of $Sr_3Mn_2O_{6+\delta}$

the anion-deficient $MnO_{1.5}$ layers are arranged in an ordered manner whereas in $Sr_3Mn_2O_{6.11}$ there is a statistical distribution of the translations connecting one bilayer to the next.

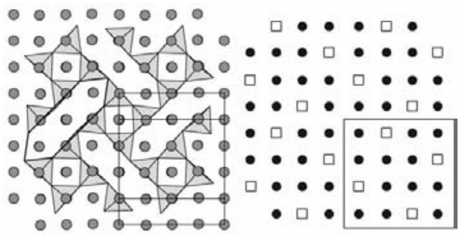

Figure 8
Projection of the model for $Sr_2MnO_{3.5}$ with at the right side the ordering pattern of the vacant oxygen chains. The triangles represent MnO_5 pyramids, the circles are Sr atoms. An elongated channel is indicated with a black outline.

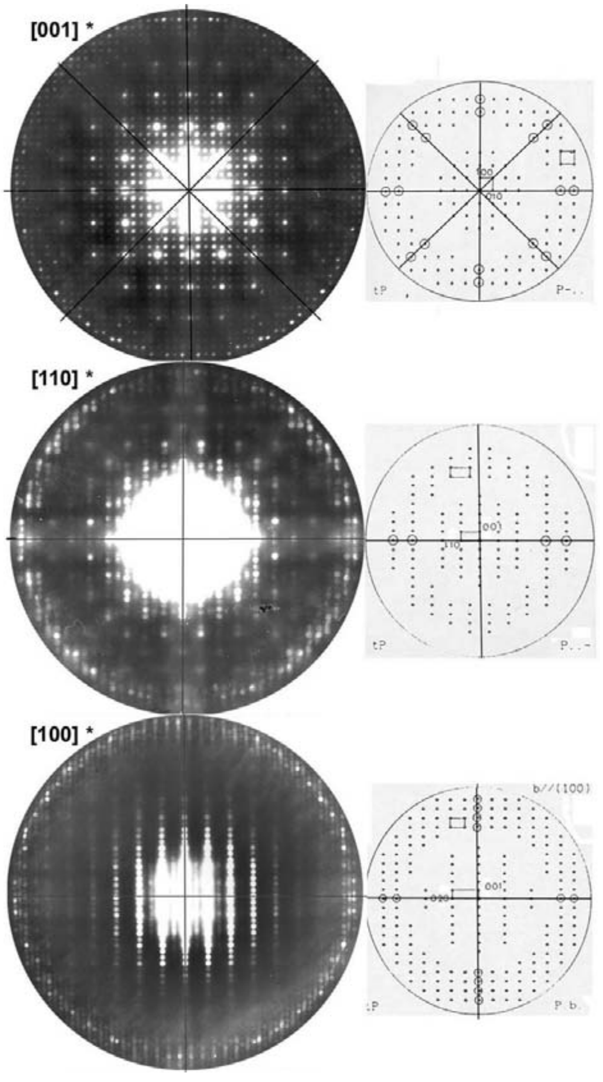

Figure 9
Microdiffraction patterns of the main zones of $Sr_3Mn_2O_{6+\delta}$. At the right side of the experimental patterns, indexing schemes corresponding to the case found in each pattern are given according to Morniroli & Steeds (1992).

Both investigations show the efficiency of TEM to detect anion ordering. Also, in many of the anion-deficient compounds described in the previous paragraph, TEM has been used to help to determine the superstructure or the correct space group for the first reported compound of a certain structural type, *e.g.* in the case of $La_{8-x}Sr_xCu_8O_{20-\delta}$ ($1.28 \leq x \leq 1.92$) (Er-Rakho *et al.*, 1988) and $(La,Ba)_5Cu_5O_{13}$ (Michel *et al.*, 1985).

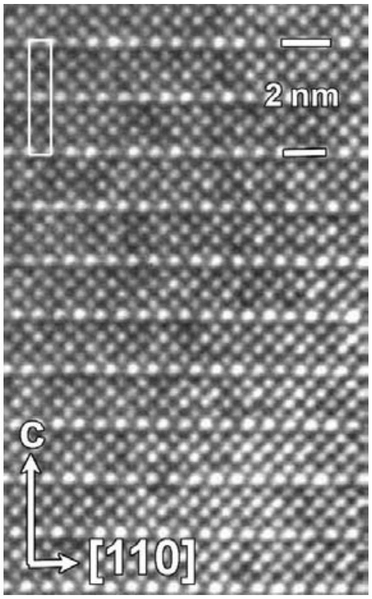

Figure 10
HREM image of $Sr_3Mn_2O_{6+\delta}$ along the $[100]_T$ direction indicating the same cation stacking as in the parent compound. No doubling of the *c* parameter is observed.

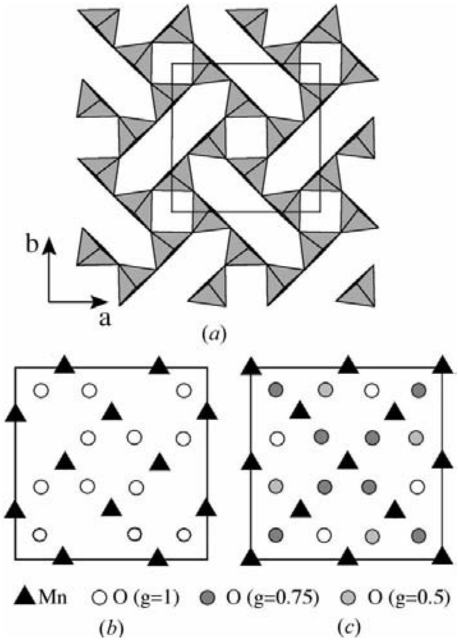

Figure 11
(*a*) Model for $Sr_3Mn_2O_{6+\delta}$, showing the proposed arrangement of MnO_5 square pyramids near $z = 0$; (*b*) the positions of the Mn and O atoms near $z = 0$; (*c*) positions and occupancies of the Mn and O atoms at $z \simeq 1/2$.

4. Fluorine incorporation into anion-deficient perovskite-like complex cuprates

Fluorine doping has proven to be an effective way to modify the crystal structure of complex oxides and tune the physical properties, *e.g.* superconductivity can be induced or T_c altered by fluorination. In cuprates, superconductivity occurs due to the presence of nearly flat infinite (CuO_2) sheets. The buckling degree of these sheets and the formal Cu oxidation state are among the most important parameters influencing the T_c value. The ordering of O atoms and vacancies is one of the parameters inducing structural distortions affecting the (CuO_2) layers and the T_c. The difference in formal charge between O and F atoms can be used to control the amount of anion vacancies and their ordering, roughly independent of the Cu oxidation state.

An important problem of fluorinated cuprates obtained by a low-temperature fluorination reaction with soft fluorinating agents (XeF_2, NH_4F, NF_3 *etc.*) is the inhomogeneity of the fluorine distribution over the sample, which causes structural differences on a local level. Examples of elaborate TEM studies showing the presence of complicated microstructures can be found for fluorinated $YBa_2Cu_3O_6F_2$ (Antipov *et al.*, 1997; Shpanchenko *et al.*, 1997), $Y_2Ba_4Cu_7O_{14}F_\delta$ (Abakumov *et al.*, 1998), $REBa_2Cu_3(O,F)_{6+\delta}$ (RE = Dy, Ho, Tm) (Oleinikov *et al.*, 2001), $La_{0.813}Sr_{0.187}Cu(O,F)_{3-\delta}$ (Abakumov *et al.*, 2000), $Nd_2Cu(O,F)_5$ (Hadermann, Van Tendeloo *et al.*, 2001), $LaHo_{0.25}Sr_{0.27}Cu(O,F)_{4+\delta}$ (Hadermann *et al.*, 1999), $La_2CuO_{3.6}F_{0.8}$ (Abakumov *et al.*, 1999), $Bi_2Sr_{1.6}La_{0.4}CuO_{6.33-x}F_{2+x}$ (Hadermann, Khasanova *et al.*, 2001).

4.1. Fluorination of $Nd_2CuO_{3.5}$

The structure of $Nd_2CuO_{3.5}$ was described by Pederzolli & Attfield (1998), and is shown in Fig. 12(*a*). This compound was fluorinated at temperatures ranging from 473 up to 673 K using XeF_2. The electron diffraction patterns of the sample fluorinated at 473 K with $Nd_2CuO_{3.5}/XeF_2$ = 1/1.3 show the presence of a main phase with a body-centered tetragonal unit cell (Fig. 13). The HREM images of the main phase exhibit a contrast similar to that observed for the T' (Nd_2CuO_4) structure, and the electron diffraction patterns of this phase can be indexed using a tetragonal unit cell with cell parameters $a_T \simeq 3.8$ and $c_T \simeq 12.2$ Å. However, ED patterns with a larger c_T parameter were also found. Analysis of a large number of ED patterns reveals that the variation in the c_T parameter for the phases in this sample occurs in a discrete manner. The c_T values can be grouped in three distinct regions: c_T = 12.2–12.4, c_T = 12.6–12.7 and c_T = 13.1–13.3 Å. The presence of these three discrete phases is evident from the inserted enlargement of the 00*l* row on the [100]* ED pattern (Fig. 13): the reflections are elongated along c_T^* and a splitting into three separate spots is observed at large *l* values. The areas with different c_T parameters exhibit a laminar appearance as shown on the low-magnification [100] image (Fig. 14). The areas with $c_T > 13$ Å are typically present as narrow bands one or two unit cells wide in a matrix of the main phase (Fig. 15).

At 473 K, the main fluorinated phase adopts the T'-type tetragonal structure. Since the material is found to be superconducting after this treatment, it is reasonable to suppose that the fluorine insertion occurs in the fluorite-type Nd_2O_2 blocks of $Nd_2CuO_{3.5}$, replacing O atoms in the tetrahedral interstices followed by a migration of the O atoms into the vacant anion sites located in the ($CuO_{1.5}\square_{0.5}$) planes. The mechanism of anion rearrangement resulting in a transformation of the monoclinic $Nd_2CuO_{3.5}$ into a tetragonal T' structure is similar to that observed in fluorinated Sr_2CuO_3 (Al-Mamouri *et al.*, 1994) (Figs. 12*a*, *b*). Calculations of the electrostatic energies for different O- and F-atom distributions between the $Nd_2(O,F)_2$ blocks and the Cu layers reveal that the driving force of this rearrangement is a gain in the elec-

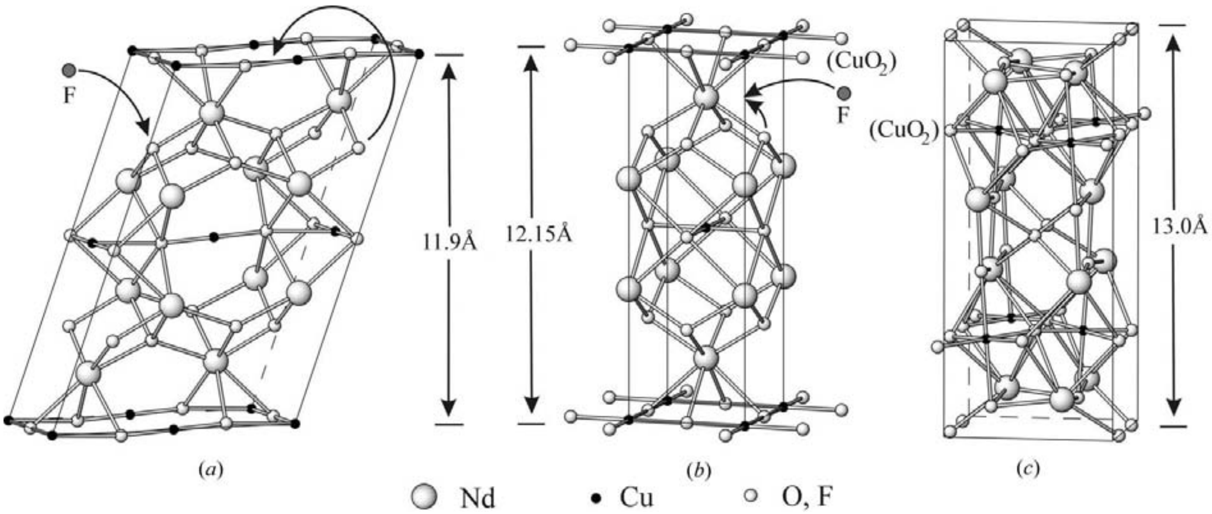

Figure 12
(*a*) Structure of $Nd_2CuO_{3.5}$ and the process of fluorine insertion into this structure; (*b*) fluorine insertion into the tetragonal main phase found at 473 K fluorination; (*c*) monoclinic phase found after 573 K fluorination. The arrows show the direction of the anion rearrangement in the structure.

trostatic energy when fluorine is located in the $Nd_2(O,F)_2$ block and oxygen is located in the Cu layers, creating (CuO_2) planes (Corbel *et al.*, 2003) (Fig. 12*b*). The extra anions expand the copper coordination environment to tetragonal pyramids and, ultimately, to octahedra. The Jahn–Teller effect leads to the elongation of the Cu—F apical bonds and an expansion of the unit cell along the c_T axis. From the ED patterns taken from bands with different c_T parameters, three different discrete $c_T/3a_T$ ratios can be calculated: 1.03, 1.07 and 1.11. These values are very close to the typical $c_T/3a_T$ ratios observed for the T', T^* and T phases of 1.02, 1.07 and 1.15, respectively (Abakumov *et al.*, 1995). The T', T^* and T phases are three related structure types that can be adopted by RE_2CuO_4 oxides (RE is a rare-earth element): the K_2NiF_4-type structure (T) with octahedrally coordinated Cu^{2+} (La_2CuO_4), the Nd_2CuO_4-type structure (T'), where the Cu ion resides in a square plane, and the T^*-type structure with square-based pyramids of CuO_5 as found in $(Nd,Ce,Sr)_2CuO_4$. The discrete values of c_T for the fluorinated tetragonal phase correspond to regions showing the three types of copper coordination found in T' (square), T^* (square pyramid) and T (octahedron) structures.

The fluorination of $Nd_2CuO_{3.5}$ at 573 K with $Nd_2CuO_{3.5}$/XeF_2 = 1/1 and 1/1.3 leads to the formation of two fluorinated phases. The first one corresponds to the fluorinated tetragonal T'-type phase, already observed in the sample fluorinated at 473 K, and a second to a monoclinic phase with lattice parameters $a_M \simeq 13.2$, $b_M \simeq 5.5$, $c_M \simeq 5.8$ Å, $\beta \simeq 92°$, and space group *C*2/*c* (Fig. 16). The tetragonal and monoclinic fluorinated phases coexist in the same crystallites, but in the sample treated at 573 K with $Nd_2CuO_{3.5}/XeF_2$ = 1/1 the monoclinic phase often forms separate crystallites. The HREM image of the monoclinic phase exhibits twins with the alternation of $[001]_M$ and $[010]_M$ oriented domains along a_M (Fig. 17). These twins appear due to the elimination of the (100) mirror plane upon the transformation from the tetragonal to the monoclinic phase.

The structure model of the monoclinic phase derived from the TEM data is shown in Fig. 12(*c*). It involves the insertion of additional F atoms into the octahedrally coordinated interstices of the $Nd_2(O,F)_2$ block, with the formation of apical bonds with the Cu atoms. When both the tetrahedral and octahedral interstices in the $Nd_2(O,F)_{2+\delta}$ block are occupied by a significant amount of anions, the anion–anion distances become close to 2–2.15 Å and strong repulsive forces lead to a structural phase transition from the tetragonal to the monoclinic $Nd_2Cu(O,F)_5$ phase. It involves an ordered occupa-

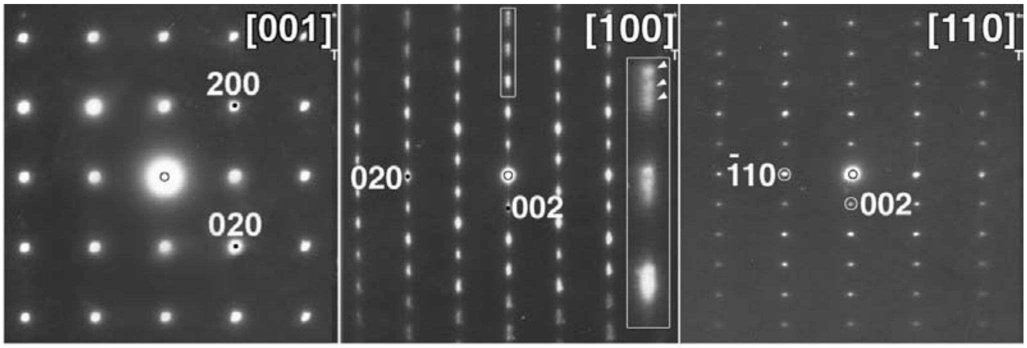

Figure 13
ED patterns of the main zones for the main phase present in $Nd_2CuO_{3.5}$ fluorinated at 473 K. The enlargement in the [100] pattern shows the splitting of the 00*l* reflections due to the presence of three phases with different degrees of fluorination.

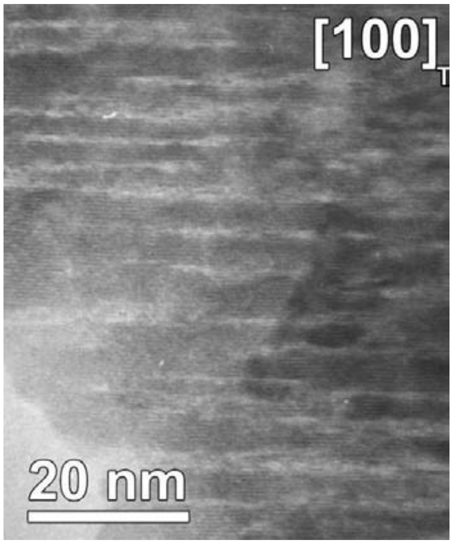

Figure 14
Low-magnification image along [100] of fluorinated $Nd_2CuO_{3.5}$, showing bands of phases with different fluorine content.

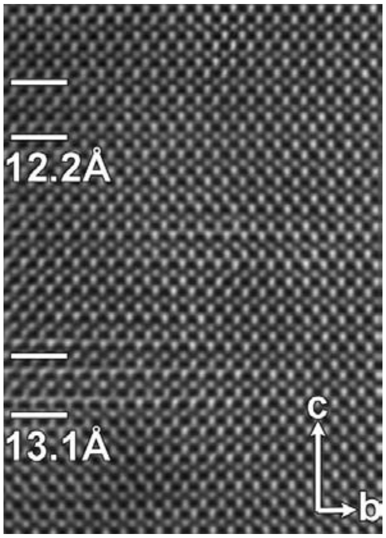

Figure 15
$[100]_T$ HREM image of the main phase in $Nd_2CuO_{3.5}$ fluorinated at 473 K showing areas with different c_T parameters.

tion of the anion sites between two adjacent Nd layers by anions and anion vacancies and the partial migration of the anions from these tetrahedrally coordinated positions to the octahedral interstices forming the apical vertexes of the $Cu(O,F)_6$ octahedra. Chains of filled and vacant tetrahedral positions run along the b_M axis and alternate along c_M. The $Cu(O,F)_6$ octahedra are tilted around b_M to maximize the distances between neighboring anions.

The transition from tetragonal to monoclinic follows the symmetry tree $I4/mmm$ ($\mathbf{a}, \mathbf{b}, \mathbf{c}$) $\rightarrow$ $Immm$ ($\mathbf{a}, \mathbf{b}, \mathbf{c}$) $\rightarrow$ $Fmmm$ ($\mathbf{a}+\mathbf{b}, \mathbf{a}-\mathbf{b}, \mathbf{c}$) $\rightarrow$ $Bbmm$ ($\mathbf{a}+\mathbf{b}, \mathbf{a}-\mathbf{b}, \mathbf{c}$) $\rightarrow$ $C2/c$ ($\mathbf{c}, \mathbf{a}+\mathbf{b}, \mathbf{a}-\mathbf{b}$). The transition from $I4/mmm$ to $Immm$ occurs due to the removal of rows of anions lying along the [110] direction, resulting in an alternation of occupied and vacant sites along $[\bar{1}10]$. The tilting of the octahedra leads to a further decrease of the symmetry to monoclinic.

These examples demonstrate how decreasing the amount of anion vacancies eliminates their ordering and the structural distortions related to this ordering. Nevertheless, in spite of the formation of the phases of higher symmetry with a smaller amount of anion vacancies, electron microscopy reveals a domain structure related to inhomogeneity in the anion distribution even within a single crystallite. The formation of such domains is not an intrinsic feature related to the symmetry properties of the anion-deficient and the anion-doped phases, but strongly depends on the sample preparation, limiting the diffusion ability of the anions.

5. Anion ordering in the $A_2MnGaO_{5+\delta}$ (A = Ca, Sr) brownmillerites

In the $A_2MnGaO_{5+\delta}$ (A = Ca, Sr) brownmillerites, a variation of oxygen stoichiometry does not significantly affect the (MnO_2) layers and mainly involves anion-deficient (GaO) layers where Ga atoms adopt a tetrahedral coordination. The specific feature determining the diversity and complexity of the brownmillerite structures is the presence of infinite chains of vertex-sharing GaO_4 tetrahedra in the (GaO) layers. These chains can be derived from the perovskite (BO_2) layers by an ordered elimination of half of the O atoms, so that the rows of filled anion positions run along $[110]_p$ and alternate with rows of vacant positions along $[\bar{1}10]_p$ (Fig. 19). The tetrahedral chains are significantly distorted due to a cooperative rotation of the tetrahedra around $[001]_p$. Tetrahedra rotated in opposite directions [clockwise (CW) and counterclockwise (CCW)] alternate along the direction of the chain propagation (Fig. 18). The tetrahedral chains can adopt two mirror-related orientations (or related by a 180° rotation), arbitrarily called left (L) and right (R). If a shift along $[\bar{1}10]_p$ transforms CW-rotated tetrahedra of one chain into CW-rotated tetrahedra of the neighboring chain, the chains are of the same sign, if the CW tetrahedra transform into CCW ones and *vice versa*, the two neighboring chains are of a different sign (L and R) (Krekels *et al.*, 1993; Milat *et al.*, 1993). In the majority of the studies, three possible arrangements of the tetrahedral chains were considered. Within the same $a \simeq a_p 2^{1/2}$, $b \simeq 4a_p$, $c \simeq a_p 2^{1/2}$ orthorhombic unit cell, the $Imma$ space group corresponds to a random arrangement of L and R chains, the $I2mb$ space group describes a structure with only one type of chain (either L or R) whereas in the $Pnma$ space group layers of L chains alternate with layers of R chains along the b axis (Fig. 19). However, the ordering of the tetrahedral chains can be much more complex than the three cases described here.

According to the powder X-ray diffraction pattern, the $Sr_2MnGaO_{5+\delta}$ phase crystallizes in a body-centered orthorhombic unit cell with lattice parameters a = 5.4056 (8), b = 16.171 (3), c = 5.5592 (7) Å (Abakumov, Rozova, Pavlyuk, Lobanov, Antipov, Lebedev, Van Tendeloo, Ignatchik *et al.*, 2001; Abakumov, Alekseeva *et al.*, 2003). However, the electron diffraction patterns show additional superlattice reflections that arise from anion ordering (Fig. 20). The brighter reflections can be indexed on a body-centered orthorhombic unit cell with the cell parameters determined from the X-ray diffraction data. Weaker spots that show up on the $[010]^*$ and $[102]^*$ patterns are satellites, which can be indexed with four $hklm$ indexes given by the diffraction vectors $\mathbf{g} = h\mathbf{a}^* + k\mathbf{b}^* + l\mathbf{c}^* + m\mathbf{q}$ with $\mathbf{q} = 1/2\mathbf{c}^*$ and the superspace group $Imma(00\gamma)s00$. According to the (3 + 1)D model proposed by Lambert *et al.* (2002), the chains in the same (GaO) layers are ordered according to the ...LRLR... sequence that is consistent with the conventional 3D $\mathbf{a}, \mathbf{b}, 2\mathbf{c}$ supercell with $Pcmb$ space symmetry (Fig. 21).

This ordering of the tetrahedral chains can be detected on the [102] HREM images, where the (GaO) layers appear as rows of bright dots, whereas other layers are represented by almost continuous white lines for this particular thickness and defocus value (Fig. 22). The (GaO) layer, consisting of chains of the same type, produces a repeat period along the layer of $\simeq$0.24 nm, whereas a doubled repeat period of $\simeq$0.48 nm is related to layers with an ...LRLR... alternation of chains along the c axis within the layer plane.

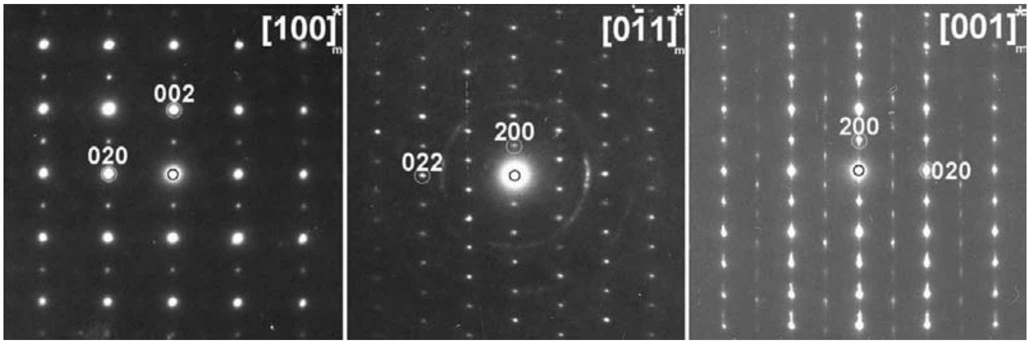

Figure 16
ED patterns of the main zones of the monoclinic $Nd_2Cu(O,F)_5$ phase obtained at 573 K fluorination.

The arrays of 0.48 nm separated dots in two neighboring (GaO) layers are shifted with respect to each other by approximately 1/4 of the interdot distance. This results in a staggered stacking of the layers, which is better visualized along the vertical line. The computer-simulated HREM image, calculated using the derived model ($\Delta f = -20$ nm, $t = 14$ nm), is shown in the inset.

The structural reasons for the different kinds of ordering of the tetrahedral chains in brownmillerites are not completely clear. Electron diffraction investigation of Sr_2MnGaO_5 at temperatures up to 1173 K *in situ* inside the electron microscope revealed that this ordering occurs well below the temperature of formation of the brownmillerite structure (Fig. 23). Around 893 K, the intensity of the satellites decreases and diffuse intensity lines appear along $\mathbf{c}^*$, passing through the basic spots. The satellites almost disappear at 938 K, but the diffuse intensity is still present. It indicates that at this temperature the long-range order of R and L chains is destroyed. At 1178 K, only the main reflections remain, and one may assume that a completely disordered structure is formed. The conditions of this experiment are close to the conditions for the preparation of Sr_2MnGaO_5 (1273 K, evacuated sealed silica tube). This allows us to deduce that the ordering of the tetrahedral chains does not take place during the solid-state reaction at 1273 K, but appears upon cooling, probably passing through a stage of short-range order.

Changing the rotation sign of the tetrahedra in the chain does not alter the interatomic distances or coordination numbers of cations within the closest coordination spheres. The L and R chains have close configurational energy, and domains with different kinds of tetrahedral chain ordering can

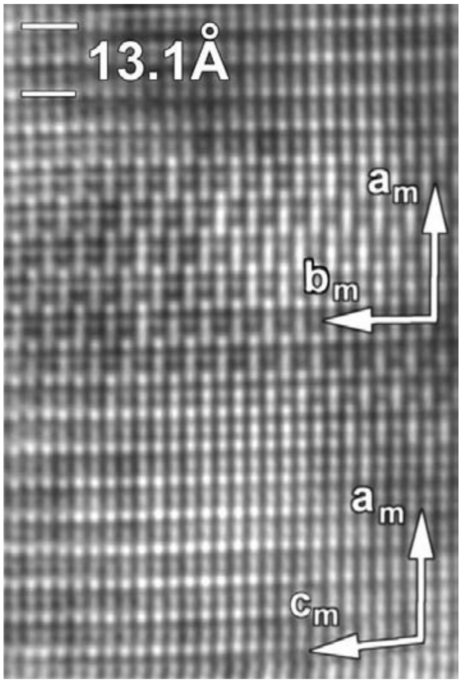

Figure 17
HREM image of the monoclinic $Nd_2Cu(O,F)_5$ phase exhibiting twins with the alternation of $[001]_M$ and $[010]_M$ oriented domains along a_M

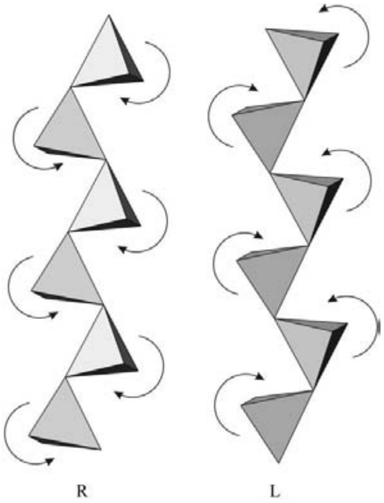

Figure 18
Two different types of tetrahedral chains (R and L) in the brownmillerite structure. Arrows show the direction of rotation of the BO_4 tetrahedra.

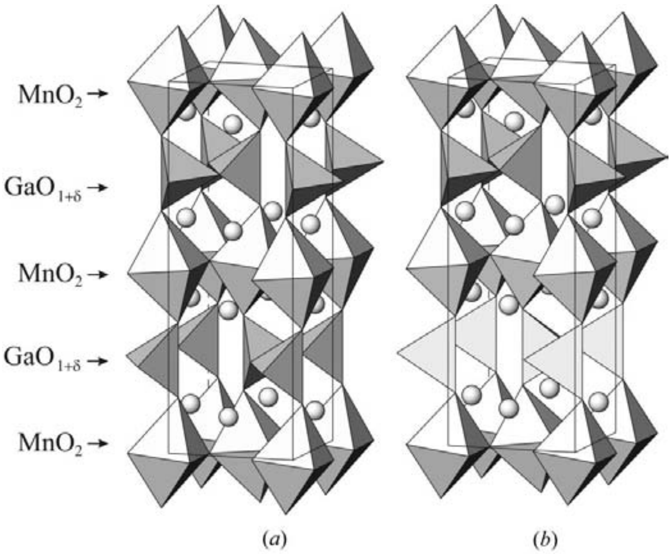

Figure 19
Crystal structures of A_2MnGaO_5 (A = Ca, Sr) brownmillerites with (*a*) *I*2*mb* and (*b*) *Pnma* space symmetry. Mn atoms are situated in octahedra, Ga atoms in tetrahedra, A cations are shown as spheres.

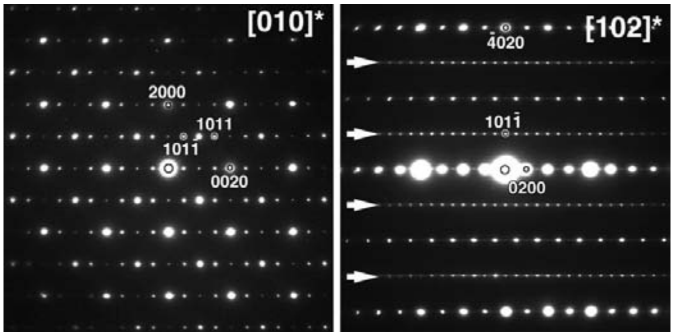

Figure 20
Electron diffraction patterns of Sr_2MnGaO_5. The rows of satellite reflections in the $[102]^*$ zone are marked by arrows. The indexing is performed with four *hklm* indexes.

be present in the structure. The samples of $Ca_2MnGaO_{5.045}$ consist of two closely intermixed brownmillerite-type phases with *Pnma* or *I2mb* space symmetry that differ mainly by the orientation of the tetrahedral chains. Fig. 24 shows [101] HREM images and the corresponding computer-simulated Fourier transforms of the crystallites exhibiting the *Pnma* (Figs. 24*a*, *b*) and the *I2mb* (Figs. 24*c*, *d*) structure, respectively. The Fourier transform corresponding to the *Pnma* symmetry (Fig. 24*a*) clearly demonstrates hkl, $k \neq 2n$, spots, which are forbidden by the *I2mb* symmetry and which are absent on the corresponding Fourier transform pattern (Fig. 24*c*). In HREM, the *Pnma* structure shows a periodicity of 15.3 Å along the *b* axis (Fig. 24*b*), whereas the visible repeat period of the *I2mb* phase is half this (Fig. 24*d*).

It often occurs for complex oxides including the CMR manganites that crystal structure refinement by means of X-ray powder data only yields an average representation of the actual structure. In the case of $Ca_2MnGaO_{5.045}$, X-ray diffraction patterns can be adequately fitted assuming a simple *Pnma* model and further details are only unveiled by electron diffraction and high-resolution electron microscopy. The reason is that the corresponding structural features involve almost exclusively the O-atom position.

Increasing the oxygen content in the $Sr_2MnGaO_{5+\delta}$ brownmillerite causes a sequence of structural changes (Abakumov, Rozova *et al.*, 2003). The increase of δ is accompanied by a gradual decrease of the orthorhombic distortion and a symmetry change from *Imma* ($0.03 \leq \delta \leq 0.13$, $a \simeq c \simeq 2^{1/2}a_p$, $b \simeq 4a_p$) to *Bmmm* ($0.41 \leq \delta \leq 0.46$, $a \simeq c \simeq 2^{1/2}a_p$, $b \simeq 2a_p$) and to tetragonal *P*4/*mmm* ($\delta = 0.505$, $a \simeq a_p$, $c \simeq 2a_p$). Oxygen insertion in the $(GaO_{1+\delta})$ layers results in the increase of the Mn oxidation state from +3 to +4 and the compression of the Mn—O apical bonds due to the suppression of the Jahn–Teller distortion of the MnO_6 octahedra. For $\delta = 0.41$, ordering of the O atoms was observed by electron diffraction, which decreases the symmetry to monoclinic *P*2/*m* ($a \simeq 10.813$, $b \simeq 8.019$, $c \simeq 8.486$ Å, $\beta \simeq 108.57°$). The reciprocal lattice for $Sr_2MnGaO_{5.41}$ was reconstructed using a large number of ED patterns, the most representative of them are shown in Fig. 25. All the brighter reflections on these patterns can be indexed with the *Bmmm* sublattice, whereas the weaker reflections correspond to the superstructure.

The [010] pattern shows a much denser array of reflections than could be expected from the proposed unit cell. The appearance of additional reflections is caused by a mirror twin with the (001) twin plane. The scheme of the formation of the [010] ED patterns as a result of two mirror-related overlapping patterns is shown in Fig. 25. Multiple diffraction results in the appearance of $h0l$ reflections with $h = 2n$, $l = n/2$. It is reasonable to propose that oxygen insertion into the $(GaO_{1+\delta})$ layers changes the coordination number of the Ga cations. A tentative structure of the $(GaO_{1+\delta})$ layers can be built compared to the structures of anion-deficient layers in the $A_2B_2O_5$ (*A* = Ca, Sr, La, *B* = Mn, Cu), $Ca_2MnO_{3.5}$ and $Sr_2MnO_{3.5}$ structures (see §2) and taking into account the compatibility with the monoclinic supercell and the *P*2/*m*

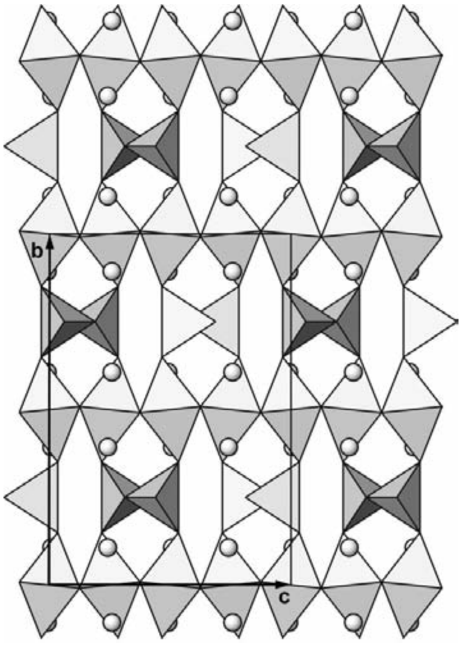

Figure 21
The crystal structure of Sr_2MnGaO_5 with an ...LRLR... type of chain alternation (*Pcmb* space symmetry). Two different projections of the GaO_4 tetrahedra correspond to two different kinds of tetrahedral chains.

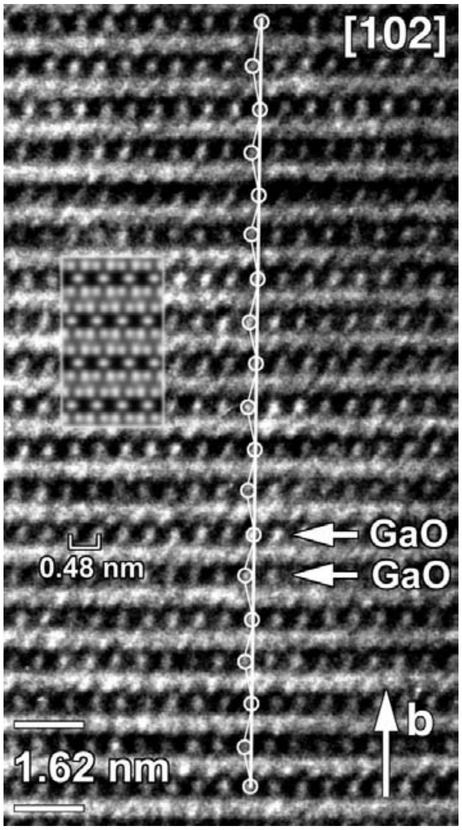

Figure 22
[102] HREM image of Sr_2MnGaO_5 reproducing the staggered stacking of the tetrahedral layers. A white vertical line is given for comparison. The theoretical HREM image calculated using the *Pcmb* structure model is shown in the inset ($\Delta f = -20$ nm, $t = 14$ nm).

space group (Fig. 26*a*). However, a tetragonal pyramid is not a typical coordination environment for the Ga^{3+} cation which is usually surrounded by 4 or 6 O atoms. In the few cases of CN = 5, Ga^{3+} cations are located in trigonal bipyramids rather than tetragonal pyramids. Hence, appropriate displacements of O and Ga atoms can be introduced to transform the coordination environment of Ga into trigonal bipyramids, as shown in Fig. 26(*b*). The obtained model corresponds to a composition $Sr_2MnGaO_{5.5}$, *i.e.* it represents a compound with ($GaO_{1.5}$) layers. The experimentally determined oxygen content is lower though and corresponds to ($GaO_{1.33}$) layers. For the given cell dimensions and the *P*2/*m* space symmetry, this leads to a partial occupation of at least one anion position in the Ga layer by O atoms and vacancies, so that some of the Ga atoms have tetrahedral coordination. The proposed model is in agreement with the experimental ED patterns, but observations in direct space by HREM are hindered by the instability of the superstructure under an intense electron beam.

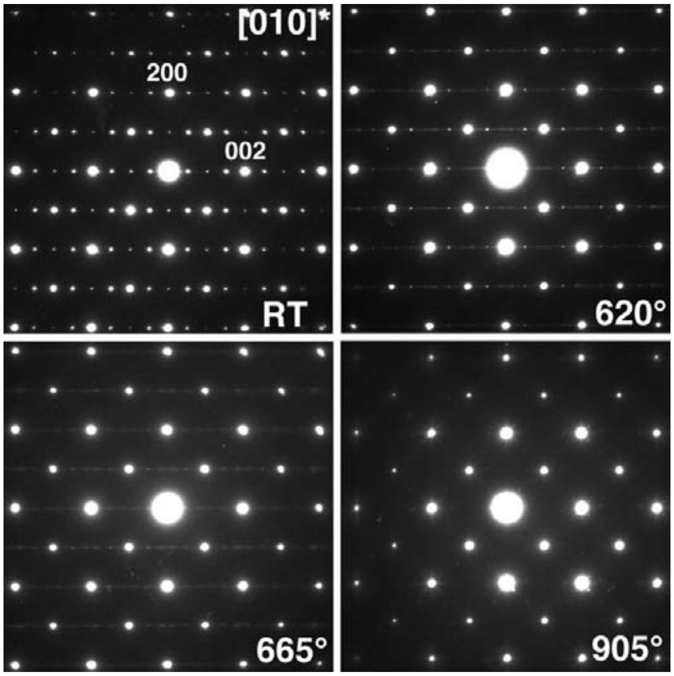

Figure 23
[010]* ED patterns of Sr_2MnGaO_5 taken at different temperatures. The intensity of the satellite reflections decreases upon increasing temperature.

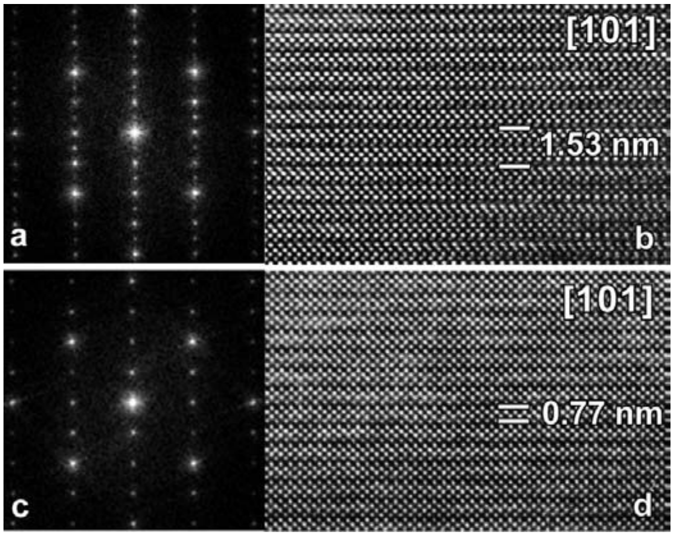

Figure 24
[101] HREM images and corresponding Fourier transform patterns of domains of well ordered (*a*), (*b*) *Pnma* and (*c*), (*d*) *I*2*mb* phases in $Ca_2MnGaO_{5.045}$. The visible repeat period for the *Pnma* phase is twice that for the *I*2*mb* phase.

Oxygen insertion into the $Ca_2MnGaO_{5+\delta}$ brownmillerite differs from that in the Sr-containing compound (Abakumov, Rozova, Pavlyuk, Lobanov, Antipov, Lebedev, Van Tendeloo, Ignatchik *et al.*, 2001). The [101] HREM image of the oxidized $Ca_2MnGaO_{5.39}$ phase (Fig. 27) shows that each second Ga-containing layer exhibits a contrast, which is nearly identical to the contrast produced by the two neighboring MnO_2 layers. It is reasonable to assume that only half of the (GaO) layers adopts extra O atoms transforming into a (GaO_2) layer whereas the other (GaO) layers remain unaffected. The (GaO) and (GaO_2) layers alternate in an ordered manner but the perfect stacking is occasionally violated by slabs with the initial *I*2*mb* structure (marked by a bracket in Fig. 27). The idealized structure of the oxygenated material can be represented by the stacking sequence –GaO_2–CaO–MnO_2–CaO–GaO–CaO–MnO_2–CaO–GaO_2– as shown in Fig. 28. The two successive Ga—O layers are no longer symmetrically connected in this structure. It can be described within the $a \simeq c \simeq a_{per}2^{1/2}$, $b \simeq 4a_{per}$ unit cell with $P2_1ma$ space group which is a non-centrosymmetric subgroup of *Pnma*. The Ga atoms in

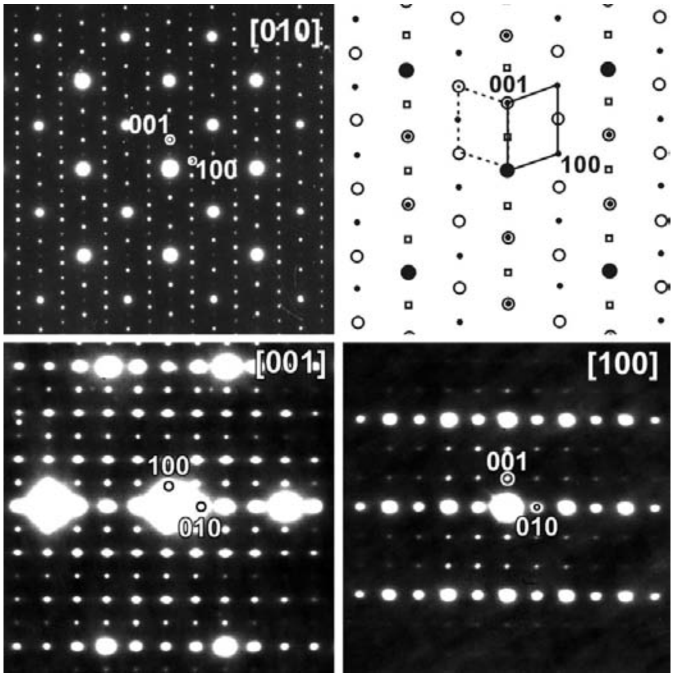

Figure 25
Electron diffraction patterns of the $Sr_2MnGaO_{5.41}$ sample. The scheme illustrating an overlap of [010] (reflections are marked as black dots) and [0$\bar{1}$0] (reflections are marked as open circles) oriented patterns is shown. The reflections arising from multiple diffraction are marked as open squares.

the (GaO_2) layers are octahedrally coordinated by six O atoms. The structure of the oxygenated $Ca_2MnGaO_{5.5} = Ca_4(Mn_2Ga)GaO_{11}$ compound may be considered as the third member of the brownmillerite $A_nB_{n-1}B'O_{3n-1}$ ($n = 4$) homologous series, in which three layers of BO_6 ($B_3 = Mn_2Ga$) octahedra form blocks separated by single layers of $B'O_4$ (B' = Ga) tetrahedra. This idealized oxygenated phase has the $Ca_2MnGaO_{5.5}$ composition, which agrees with the oxygen non-stoichiometry $\delta = 0.39$ if the presence of some reduced *I2mb* blocks is taken into account. The HREM simulated image shown as inset in Fig. 27 and calculated using this model ($\Delta f = -600$ Å, $t = 30$ Å) shows remarkable agreement with the experimental image.

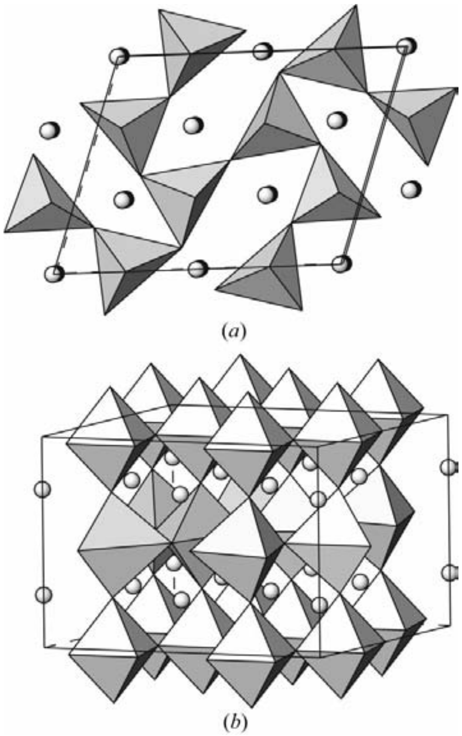

Figure 26
The model of $Sr_2MnGaO_{5.41}$ structure: (*a*) the structure of the Ga layer; (*b*) three-dimensional view. Mn atoms are situated in octahedra, Ga atoms in trigonal bipyramids, O atoms are at the corners of the polyhedra, Sr cations are shown as spheres.

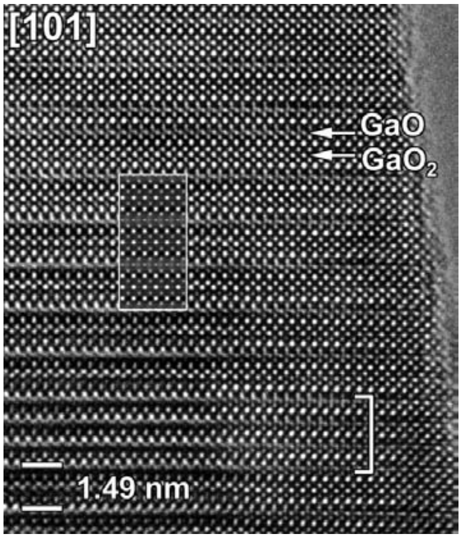

Figure 27
[101] HREM image of $Ca_2MnGaO_{5.39}$ material. The (GaO) and (GaO_2) layers are marked. The slab of *I2mb* structure is marked by a bracket. The image, calculated using $Ca_2MnGaO_{5.5}$ model ($\Delta f = -600$ Å, $t = 30$ Å), is shown in the insert.

6. Conclusions

Several examples of structural transformations due to a variation of the anion content in perovskite-like complex Mn- and Cu-containing oxides show that such materials can have a complicated microstructure which has to be taken into account for a complete structural characterization. The compounds prepared using oxidation, reduction at low temperature or fluorine insertion are fragmented into domains. The domain structure arises as a consequence of the decrease of symmetry due to the ordering of anions and vacancies in the anion-deficient phase in comparison with the parent compound with filled anion positions. Also the insertion of extra anions is accompanied by the formation of domains due to local inhomogeneity in the anion distribution over the sample. In the stoichiometric brownmillerite structure there is more than one possibility for an ordered arrangement of O atoms and vacancies, and the free energy of these ordered variants can be estimated as very close. The final stage of the thermal treatment during the preparation of such phases plays a key role in the resulting microstructure which consists of domains with structures that differ by anion ordering. Owing to the low sensitivity of conventional laboratory powder X-ray diffraction to such light scatterers as

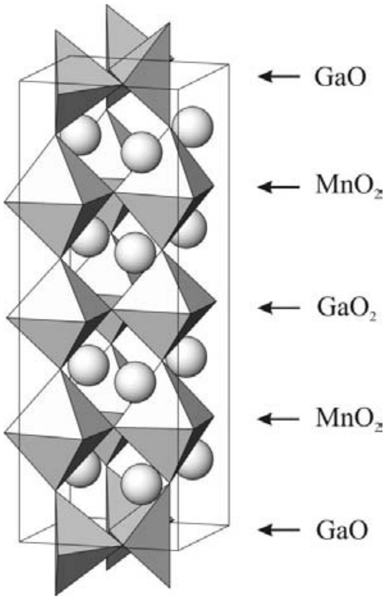

Figure 28
Structure model of the oxidized $Ca_2MnGaO_{5.5}$ phase. Ga and Mn atoms are at the centers of the polyhedra, O atoms are at the corners, Ca cations are shown as spheres.

O (or F) atoms, the ability of this technique to detect the superstructure arising from anion ordering is rather limited. In some cases, as was shown for $Sr_2MnO_{3.5}$, the deformation of the subcell is also below the resolution limit of the laboratory diffractometer, so that the monoclinic distorted structure of $Sr_2MnO_{3.5}$ was initially interpreted as being tetragonal. Fragmentation of the structure into domains of a small size makes the situation even more complicated. In such cases, electron diffraction and high-resolution electron microscopy investigation play a key role for building an initial structure model for the Rietveld refinement from X-ray and neutron powder diffraction data.

The authors are grateful to O. I. Lebedev and L. Gillie for useful collaboration. The work was supported in part by program IAP V-1 of the Belgium government. Acknowledgment is made to the donors of the American Chemical Society Petroleum Research Fund for partial support of this research (project 38459-AC5). AMA is grateful to INTAS for the Fellowship Grant for Young Scientists YSF 03-55-1035 and to the Russian Science Support Foundation for financial support

References

Abakumov, A. M., Alekseeva, A. M., Rozova, M. G., Antipov, E. V., Lebedev, O. I., Van Tendeloo, G. (2003). *J. Solid State Chem.* **174**, 319–325.

Abakumov, A. M., Antipov, E. V., Kovba, L. M., Kopnin, E. M., Putilin, S. N. & Shpanchenko, R. V. (1995). *Russ. Chem. Rev.* **64**, 719–729.

Abakumov, A. M., Hadermann, J., Rozova, M. G., Pavljuk, B. Ph., Antipov, E. V., Lebedev, O. I. & Van Tendeloo, G. (2000). *J. Solid State Chem.* **149**, 189–196.

Abakumov, A. M., Hadermann, J., Van Tendeloo, G., Shpanchenko, R. V., Oleinikov, P. N. & Antipov, E. V. (1999). *J. Solid State Chem.* **142**, 440–450.

Abakumov, A. M., Rozova, M. G., Alekseeva, A. M., Kovba, M. L., Antipov, E. V., Lebedev, O. I. & Van Tendeloo, G. (2003). *Solid State Sci.* **5**, 871–882.

Abakumov, A. M., Rozova, M. G., Ardashnikova, E. I. & Antipov, E. V. (2002). *Russ. Chem. Rev*. **71**, 383–399.

Abakumov, A. M., Rozova, M. G., Pavlyuk, B. P., Lobanov, M. V., Antipov, E. V., Lebedev, O. I., Van Tendeloo, G., Ignatchik, O. L., Ovtchenkov, E. A., Koksharov, Y. A. & Vasil'ev, A. N. (2001). *J. Solid State Chem.* **160**, 353–361.

Abakumov, A. M., Rozova, M. G., Pavlyuk, B. P., Lobanov, M. V., Antipov, E. V., Lebedev, O. I., Van Tendeloo, G., Sheptyakov, D. V., Balagurov, A. M. & Bourée, F. (2001). *J. Solid State Chem.* **158**, 100–111.

Abakumov, A. M., Rozova, M. G., Shpanchenko, R. V., Kovba, M. L., Putilin, S. N., Antipov, E. V., Lebedev, O. I., Van Tendeloo, G., Kopnin, E. M. & Karpinski, J. (1998). *Physica (Utrecht)*, C**301**, 155–164.

Al-Mamouri, M., Edwards, P. P., Greaves, C. & Slaski, M. (1994). *Nature (London)*, **369**, 382.

Amamoto, Y., Yamane, H. & Hirai, T. (1996). *J. Solid State Chem.* **125**, 117–124.

Anderson, M. T., Vaughey, J. T. & Poeppelmeier, K. R. (1993). *Chem. Mater.* **5**, 151–165.

Anderson, P. S., Kirk, C. A., Skakle, J. M. S. & West, A. R. (2003). *J. Solid State Chem.* **170**, 1–8.

Antipov, E. V., Putilin, S. N., Shpanchenko, R. V., Alyoshin, V. A., Rozova, M. G., Abakumov, A. M., Mikhailova, D. A., Balagurov, A. M., Lebedev, O. I. & Van Tendeloo, G. (1997). *Physica (Utrecht)*, C**282–287**, 61–64.

Batson, P. E. (1993). *Nature (London)*, **366**, 728.

Battle, P. D., Bell, A. M. T., Blundell, S. J., Coldea, A. I., Gallon, D. J., Pratt, F. L., Rosseinsky, M. J. & Steer, C. A. (2002). *J. Solid State Chem.* **167**, 188–195.

Blundell, S. J., Marshall, I. M., Pratt, F. L., Hayward, M. A., Cussen, E. J., Claridge, J. B., Bieringer, M., Kiely, C. J. & Rosseinsky, M. J. (2003). *Physica (Utrecht)*, B**326**, 527–531.

Browning, N. D., Chisholm, M. M. & Pennycook, S. J. (1993). *Nature (London)*, **366**, 143–143.

Burdett, J. K. & Kulkarni, G. V. (1988). *J. Am. Chem. Soc.* **110**, 5361–5368.

Caignaert, V., Hervieu, M. & Raveau, B. (1986). *Mater. Res. Bull.* **21**, 1147–1154.

Caignaert, V., Nguyen, N., Hervieu, M. & Raveau, B. (1985). *Mater. Res. Bull.* **20**, 479–484.

Cava, R. J., Zandbergen, H. W., Van Dover, R. B., Krajewski, J. J., Siegrist, T., Peck W. F. Jr, Roth, R. S. & Felder, R. J. (1994). *J. Solid State Chem.* **109**, 345–351.

Corbel, G., Attfield, J. P., Hadermann, J., Abakumov, A. M., Alekseeva, A. M., Rozova, M. G. & Antipov, E. V. (2003). *Chem. Mater.* **15**, 189–195.

Er-Rakho, L., Michel, C. & Raveau, B. (1988). *J. Solid State Chem.* **73**, 514–519.

Fu, W. T., Ijdo, D. J. W. & Helmholdt, R. B. (1992). *Mater. Res. Bull.* **27**, 287–293.

Fujishita, H., Sera, M. & Sato, M. (1991). *Physica (Utrecht)*, C**175**, 165–171.

Genouel, R., Michel, C., Nguyen, N., Hervieu, M. & Raveau, B. (1995). *J. Solid State Chem.* **115**, 469–475.

Gillie, L. J., Palmer, H. M., Wright, A. J., Hadermann, J., Van Tendeloo, G. & Greaves, C. (2004). *J. Phys. Chem. Solids*, **65**, 87–93.

Gillie, L. J., Wright, A. J. Hadermann, J., Van Tendeloo, G. & Greaves, C. (2002). *J. Solid State Chem.* **167**, 145–151.

Gillie, L. J., Wright, A. J., Hadermann, J., Van Tendeloo, G. & Greaves, C. (2003). *J. Solid State Chem.* **175**, 188–196.

Hadermann, J., Abakumov, A. M., Lebedev, O. I., Van Tendeloo, G., Rozova, M. G., Shpanchenko, R. V., Pavljuk, B. P., Kopnin, E. M. & Antipov, E. V. (1999). *J. Solid State Chem.* **147**, 647–656.

Hadermann, J., Khasanova, N. R., Van Tendeloo, G., Abakumov, A. M., Rozova, M. G., Alekseeva, A. M. & Antipov, E. V. (2001). *J. Solid State Chem.* **156**, 445–451.

Hadermann, J., Van Tendeloo, G., Abakumov, A. M., Rozova M. G. & Antipov, E. V. (2001). *J. Solid State Chem.* **157**, 56–61.

Hayward, M. A., Cussen, E. J., Claridge, J. B., Bieringer, M., Rosseinsky, M. J., Kiely, C. J., Blundell, S. J., Marshall, I. M. & Pratt, F. L. (2002). *Science*, **295**, 1882–1882.

Hiroi, Z. (1996). *J. Solid State Chem.* **123**, 223–235.

Karppinen, M. & Yamauchi, H. (2000). *Int. J. Inorg. Mater.* **2**, 589–599.

Kato, S., Nakahara, Y., Sugai, M., Ohshima, Y. & Makino, K. (1997). *Mater. Lett.* **30**, 163–167.

Khasanova, N. R., Izumi, F., Hewat, A. W. & Takayama-Muromachi, E. (1996). *Physica (Utrecht)*, C**258**, 227–235.

Klie, R. F. & Browning, N. D. (2002). *J. Electron. Microsc.* **51**, S59–S66.

Klie, R. F., Ito, Y., Stemmer, S. & Browning, N. D. (2001). *Ultramicroscopy*, **86**, 289–302.

Krekels, T., Milat, O., Van Tendeloo, G., Amelinckx, S., Babu, T. G. N., Wright, A. J. & Greaves, C. (1993). *J. Solid State Chem.* **105**, 313–335.

Kriegel, R. & Feltz, A. (1992). *Z. Anorg. Allg. Chem.* **617**, 99.

Lambert, S., Leligny, H., Grebille, D., Pelloquin, D. & Raveau, B. (2002). *Chem. Mater.* **14**, 1818–1826.

Leligny, H., Grebille, D., Hervieu, M. & Martin, C. (2003). Poster communication, Association Française de Cristallographie.

Lokshin, K. A., Pavlov, D. A., Putilin, S. N., Antipov, E. V., Sheptyakov, D. V. & Balagurov, A. M. (2001). *Phys. Rev. B*, **63**, 64511.

Matsui, Y. & Akimitsu, J. (1995). *Microsc. Res. Tech.* **30**, 155–166.

Michel, C., Er-Rakho, L., Hervieu, M., Pannetier, J. & Raveau, B. (1987). *J. Solid State Chem.* **68**, 143–152.

Michel, C., Er-Rakho L. & Raveau, B. (1985). *Mater. Res. Bull.* **20**, 667–671.

Milat, O., Krekels, T., Van Tendeloo, G. & Amelinckx, S. (1993). *J. Phys. (Paris) I*, **3**, 1219–1234.

Mitchell, J. F., Millburn, J. E., Medarde, M., Short, S. & Jorgensen, J. D. (1999). *J. Appl. Phys.* **85**, 4352–4354.

Morniroli, J. P. & Steeds, J. W. (1992). *Ultramicroscopy*, **45**, 219–239.

Muller, D. A. & Mills, M. J. (1999). *Mater. Sci. Eng.* A**260**, 12–28.

Muller, D. A., Subramanian, S., Sass, S. L., Silcox, J. & Batson, P. E. (1995). *Phys. Rev. Lett.* **75**, 4744–4747.

Muller, D. A., Tzou, Y. Raj, R. & Silcox, J. (1993). *Nature (London)*, **366**, 725.

Oleinikov, P. N., Shpanchenko, R. V., Rozova, M. G., Abakumov, A. M., Antipov, E. V., Hadermann, J., Lebedev, O. I. & Van Tendeloo, G. (2001). *Russ. J. Inorg. Chem.* **46**, 153–158.

Otzschi, K., Hayashi, A., Fujiwara, Y. & Ueda, Y. (1993). *J. Solid State Chem.* **105**, 573–579.

Otzschi, K., Koga, K. & Ueda, Y. (1995). *J. Solid State Chem.* **115**, 490–498.

Otzschi, K. & Ueda, Y. (1993). *J. Solid State Chem.* **107**, 149–158.

Parras, M., Alonso, J., Gonzales-Calbet, J. M. & Vallet-Regi, M. (1995). *J. Solid State Chem.* **117**, 21–29.

Pederzolli, D. R. & Attfield, J. P. (1998). *J. Solid State Chem.* **136**, 137–140.

Poeppelmeier, K. R., Leonowicz, M. E. & Longo, J. M. (1982). *J. Solid State Chem.* **44**, 89–98.

Portier, R. & Gratias, D. (1982). *J. Phys. (Paris)*, **43**, C4.

Rangavittal, N., Subbanna, G. N., Guru Row, T. N. & Rao, C. N. R. (1995). *J. Solid State Chem.* **114**, 95–101.

Raveau, B., Michel, C. & Hervieu, M. (1989). *Solid State Ionics*, **32–33**, 1035–1042.

Reller, A., Davoodabady, G. & Oswald, H. R. (1985). *Thermochim. Acta*, **83**, 121–124.

Reller, A., Thomas, J. M., Jefferson, D. A. & Uppal, M. K. (1984). *Proc. R. Soc. London Ser. A*, **394**, 223.

Roberts, G. L., Cava, R. J., Carter, S. A., Krajewski, J. J. & Peck, W. F. Jr (1996). *J. Solid State Chem.* **121**, 319–323.

Roth, G., Adelmann, P., Knitter, R., Massing, S. & Wolf, Th. (1992). *J. Solid State Chem.* **99**, 376.

Salje, E. K. H. (1990). *Phase Transitions in Ferroelastic and Co-elastic Crystals*. Cambridge University Press.

Shivakumara, C., Hegde, M. S., Rajagopal, H. & Sequiera, A. (2000). *Mater. Res. Bull.* **35**, 2063–2068.

Shivakumara, C., Hegde, M. S., Sooryanarayana, K., Row, T. N. G. & Subbanna, G. N. (1998). *J. Solid State Chem.* **8**, 2695–2700.

Shpanchenko, R. V., Rozova, M. G., Abakumov, A. M., Ardashnikova, E. I., Kovba, M. L., Putilin, S. N., Antipov, E. V., Lebedev, O. I. & Van Tendeloo, G. (1997). *Physica (Utrecht)*, C**280**, 272–280.

Siegrist, T., Zahurak, S. M., Murphy, D. W. & Roth, R. S. (1988). *Nature (London)*, **334**, 231–232.

Sinnott, S. B. & Dickey, E. C. (2003). *Mater. Sci. Eng. Rep.* **43**, 1–59.

Spence, J. C. H. (1999). *Mater. Sci. Eng. Rep.* **26**, 1–49.

Stemmer, S., Sane, A., Browning, N. D. & Mazanec, T. J. (2000). *Solid State Ionics*, **130**, 71–80.

Takano, M., Azuma, M., Hiroi, Z., Bando, Y. & Takeda, Y. (1991). *Physica (Utrecht)*, C**176**, 441–444.

Teske, C. L. & Mueller-Buschbaum, H. K. (1969). *Z. Anorg. Allg. Chem.* **371**, 325.

Van Tendeloo, G. & Amelinckx, S. (1974). *Acta Cryst.* A**30**, 431–440.

Van Tendeloo, G., Lebedev, O. I., Shpanchenko, R. V. & Antipov, E. V. (1997). *J. Electron Microsc. (Tokyo)*, **46**, 23–31.

Vaughey, J. T., Wiley, J. B. & Poeppelmeier, K. R. (1991). *Z. Anorg. Allg. Chem.* **598/599**, 321.

Wright, A. J., Palmer, H. M., Anderson, P. A. & Greaves, C. (2001). *J. Mater. Chem.* **11**, 1324–1326.

Wright, A. J., Palmer, H. M., Anderson, P. A. & Greaves, C. (2002). *J. Mater. Chem.* **12**, 978–982.